Biochemistry

pubs.acs.org/biochemistry Article

Characterization of Conformational Dynamics and Structural Plasticity of the Catalytic Domain of Human Mitochondrial YME1L Protease

Megan K. Black,[#] Angelina Kim,[#] Ching Y. Chen, Monica M. Goncalves, Simrah Waseem, Siavash Vahidi,[*] and Rui Huang[*]

Cite This: https://doi.org/10.1021/acs.biochem.5c00535 Read Online

ACCESS | Metrics & More | Article Recommendations | Supporting Information

ABSTRACT: Mitochondrial proteostasis is essential to maintain cellular function and survival. YME1L is a membrane-anchored AAA+ (ATPases Associated with diverse cellular Activities) family protease and plays a pivotal role in mitochondrial proteostasis by selectively degrading misfolded and native proteins. The precise mechanisms by which nucleotide binding and hydrolysis influence YME1L's conformational dynamics, proteolytic activity, and stability remain unclear. Here, we characterize the conformational dynamics of the YME1L catalytic domain. Using a hexameric soluble YME1L construct, we employ hydrogen/deuterium exchange mass spectrometry (HDX-MS) and nuclear magnetic resonance (NMR) spectroscopy to demonstrate that nucleotide binding reduces the backbone flexibility and modulates the side-chain dynamics of the AAA+ domain, while Zn^{2+} binding stabilizes the protease domain. We also reveal long-range functional crosstalk between the AAA+ and protease domains of YME1L. We use functional assays to show the importance of a salt bridge between the AAA+ and protease domains in facilitating ATP-dependent substrate degradation by YME1L. Additionally, we show that ATP binding stabilizes the structure of the catalytic domain of YME1L and protects it from chemical- and heat-induced aggregation. These findings explain the nucleotide-driven regulation of YME1L and provide insights into our understanding of its proteolytic activity and structural stability under stress conditions.

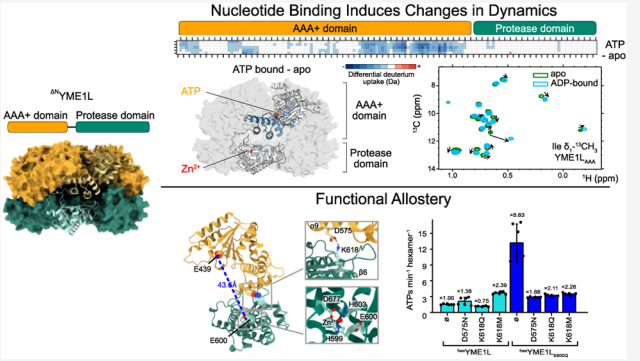

Mitochondria contain approximately 1,100 unique proteins, with all but 13 encoded by nuclear DNA and translated in the cytoplasm.[1,2] These proteins are imported into the mitochondria, processed, and folded into their functional forms, while their quality is maintained by a complex network of pathways that regulate biosynthesis, import, folding, degradation, and mitophagy.[3] This quality control system is essential for mitochondrial functionality and overall cell survival, as improper protein folding can lead to toxic aggregation. A key aspect of this quality control involves degradation of misfolded mitochondrial proteins, a process mediated by a family of AAA+ (ATPases Associated with diverse cellular Activities) proteases found in all mitochondrial compartments.[4,5] These proteases use energy from ATP hydrolysis to unfold and degrade protein substrates.

One such mitochondrial protease, YME1L, belongs to the AAA+ family and localizes to the inner mitochondrial membrane (IM), with its catalytic domain extending into the intermembrane space (IMS). YME1L is a hexameric complex, with each subunit containing an N-terminal domain, a single transmembrane helix, followed by a catalytic domain that is soluble in the absence of the transmembrane domain. The catalytic domain consists of a AAA+ (ATPases Associated with diverse cellular Activities) domain and a Zn^{2+}-dependent metalloprotease domain (Figure 1A and B).[6,7] The AAA+ domain of YME1L harnesses the chemical energy from ATP hydrolysis to drive unfolding and translocation of substrates through the central pore of the enzyme and into the protease domain for degradation.[8] YME1L plays a vital role in maintaining mitochondrial proteostasis. Disruption of YME1L function leads to mitochondrial dysfunction and reduced cell survival under stress conditions.[9,10] YME1L is upregulated in several cancers, making it a promising target for cancer diagnosis and therapeutics.[11−14] YME1L removes aberrant proteins from the IM and IMS, such as the unassembled subunits of respiratory Complex I (*e.g.*,

Received: September 2, 2025
Revised: December 31, 2025
Accepted: February 13, 2026

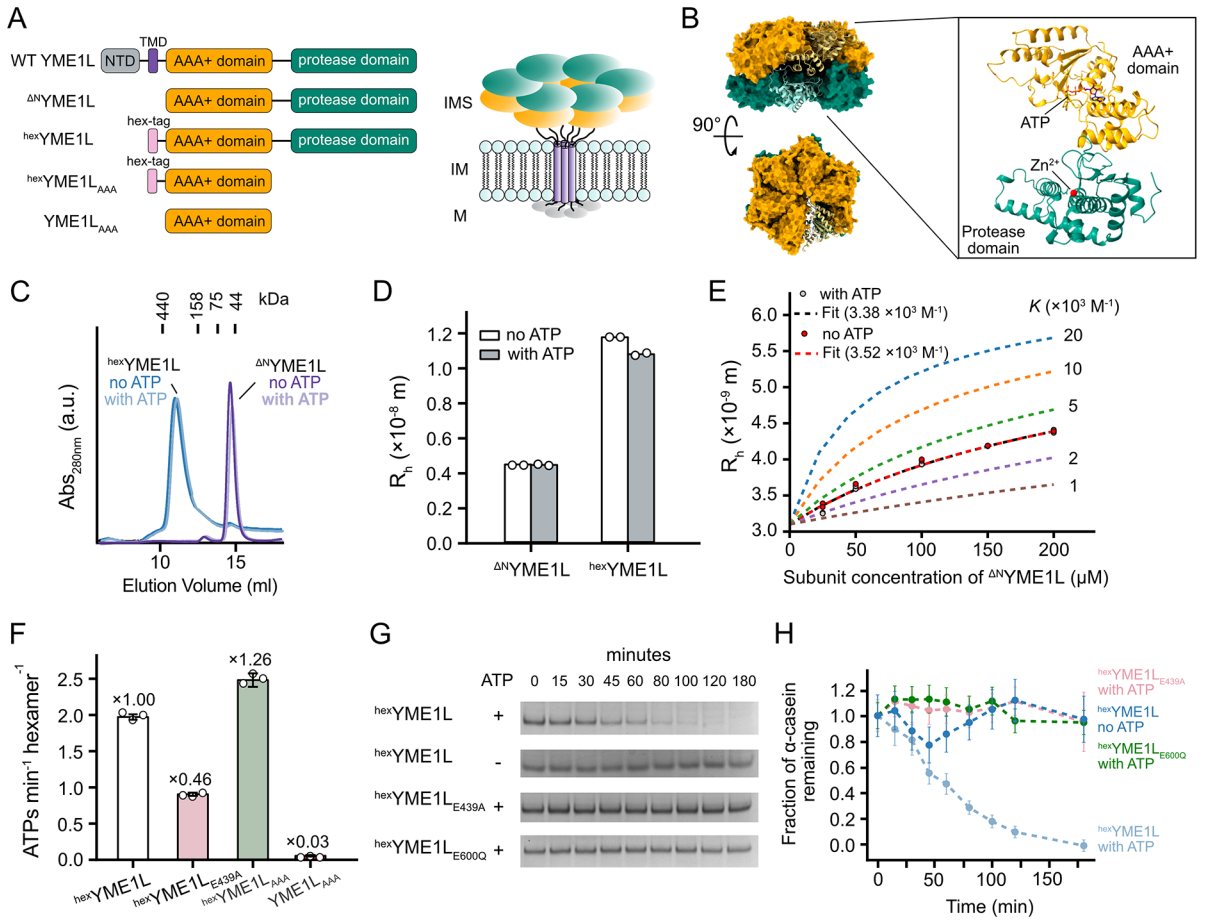

Figure 1. Oligomerization and enzymatic activity of the catalytical domain of YME1L in the presence of a hex-tag. (A) Left: Domain organization of a WT YME1L subunit (WT YME1L) and cartoon representations of the YME1L constructs used in the study. Right: Schematic representation of the hexameric YME1L anchored to the inner membrane of mitochondria (M = mitochondrial matrix; IM = mitochondrial inner membrane; IMS = mitochondrial intermembrane space). (B) Structural model of the hexameric catalytic domain (residues 317−773) of YME1L, predicted by AlphaFold3,[15] featuring two distinct layers—the AAA+ domains (dark yellow) and the protease domains (dark green), together enclosing the central pore. The predicted structure of a monomer bound to ATP and Zn^{2+} is enlarged. (C) SEC elution profiles of ^{hex}YME1L and $^{\Delta N}$YME1L in the presence and absence of 5 mM ATP. The molecular weights of the standards are given along the top. (D) Hydrodynamic radii of ^{hex}YME1L and $^{\Delta N}$YME1L in the presence and absence of 10 mM ATP obtained by dynamic light scattering. Data were measured at a subunit concentration of 200 μM, 15 °C. (E) Hydrodynamic radii of $^{\Delta N}$YME1L as a function of concentration in the presence (gray circles) and absence (red circles) of 10 mM ATP, measured by DLS at 15 °C. Dashed lines represent simulated curves generated using the model described in *Materials and Methods*, with the microscopic association constant (K) ranging from 1×10^{-3} to 20×10^{-3} M^{-1}. (F) Rate of ATP hydrolysis by ^{hex}YME1L, ^{hex}YME1L$_{E439A}$ (Walker-B variant), ^{hex}YME1L$_{AAA}$, and monomeric YME1L$_{AAA}$. Normalized ATPase activities with respect to those of ^{hex}YME1L are denoted above the bars. (G) Degradation of α-casein by ^{hex}YME1L, ^{hex}YME1L$_{E439A}$, and ^{hex}YME1L$_{E600Q}$ (protease-inhibiting variant). (H) The fraction of remaining α-casein over time in the degradation assays shown in (F). Errors are calculated based on technical triplicates. Images of the uncropped SDS-PAGE gels are shown in Figure S2.

NDUFB6 and ND1) and Complex IV (*e.g.*, COX4),[4,6,16] and degrades specific native mitochondrial proteins to adapt to cellular stress. Under stress conditions, YME1L degrades TIMM17A, a component of the protein translocase TIM23 complex in the IM, to reduce protein import into the mitochondria.[17] Additionally, YME1L regulates mitochondrial morphology by processing OPA1, a dynamin-like protein, which exists in both a long membrane-bound form (L-OPA1) and a soluble short form (S-OPA1) in the mitochondria.[18] The balance between these two forms is crucial for maintaining mitochondrial morphology.[19−21] YME1L and the ATP-independent protease OMA1 cleave L-OPA1 to produce S-OPA1, particularly under stress conditions such as membrane depolarization and oxidative stress, promoting mitochondrial fission.[22−24] On the other hand, high ATP levels activate YME1L to degrade OMA1, counteracting OMA1-induced mitochondrial fragmentation, while depletion of ATP leads to inactivation of YME1L, allowing it to be reciprocally degraded by OMA1.[9] ATP binding has been shown to stabilize YME1L, protecting it from hydrogen peroxide-induced modification and degradation by OMA1.[9,25] However, the precise mechanisms by which nucleotide binding and hydrolysis affect YME1L's conformational dynamics and stability are not fully understood.

Here, we present a detailed characterization of the conformational dynamics, structural plasticity, and stability of the catalytic domain of YME1L. Using size-exclusion chromatography (SEC) and dynamic light scattering (DLS), we demonstrate that the isolated soluble domain of YME1L has a low propensity to oligomerize. Using a hexameric soluble construct of YME1L, we characterize the nucleotide- and Zn^{2+}-induced changes in conformational dynamics using a

https://doi.org/10.1021/acs.biochem.5c00535
Biochemistry XXXX, XXX, XXX−XXX

combination of hydrogen/deuterium exchange mass spectrometry (HDX-MS) and nuclear magnetic resonance (NMR) spectroscopy. Our results show that ATP and ADP binding significantly reduce backbone flexibility in the AAA+ domain, while Zn^{2+} binding leads to the rigidification of the protease domain. ADP binding also modulates the side-chain dynamics of the AAA+ domain. Furthermore, we uncover long-range functional crosstalk between the AAA+ and protease domains, highlighting the structural plasticity of YME1L. Finally, we demonstrate that ATP binding enhances YME1L's thermal stability and protects it from aggregation due to chemical modification, thereby demonstrating the stabilization effect of nucleotide binding on the structure and folding of YME1L. Our findings offer insights into how nucleotide binding modulates YME1L's conformational dynamics and stability in vitro.

MATERIALS AND METHODS

Cloning, Protein Expression, and Purification

The expression plasmid of ^{hex}YME1L from *Homo sapiens* in a PET24 vector was a gift from Dr. Justin Miller (Middle Tennessee State University), which encodes a YME1L construct that contains an N-terminal His_6-tag followed by SUMO (Small Ubiquitin-like Modifier), a hex-tag (GELKAIAQELKAIAKELKAIAWELKAIAQGAG),[6] and the catalytical domain of YME1L (residues 317−773), connected with a 10-aa linker (GSGSYFQSNA). All other YME1L constructs used in the study were generated from the ^{hex}YME1L construct using the QuikChange site-directed mutagenesis method with Phusion DNA polymerase (New England Biolabs). The $^{hex}YMEL_{AAA}$ construct contains a hex-tag connected to residues 317−588 of YME1L via the same 10-aa linker. Oligonucleotides used for molecular cloning were synthesized by Integrated DNA Technologies (IDT). Plasmids were prepared by transforming the QuikChange product into the NEB Turbo Competent *E. coli* cells and miniprepped using the NEB Monarch Plasmid Miniprep Kit. All of the plasmids were sequenced by Plasmidsaurus to confirm the fidelity of the constructs.

All the YME1L constructs were expressed in *E. coli* strain BL21 (DE3) cells. Cells were grown in the LB broth with 50 μg/mL kanamycin at 37 °C until induction at OD_{600} = 0.6 with 0.25 mM isopropyl β-d-1-thiogalactopyranoside (IPTG). Protein expression was carried out at 25 °C for ca. 16 h. To express [Ile (δ_1), Leu (δ_1,δ_2), Val (γ_1,γ_2), Met (ε)-$^{13}CH_3$]-labeled $YME1L_{AAA}$ and $^{\Delta N}$YME1L, M9 minimal media in 99% D_2O with d_7-glucose as the sole carbon source was used. Selective methyl labeling was achieved, as previously described,[26] by adding 100 mg/L ε-[$^{13}CH_3$]-labeled methionine (CLM-206; Cambridge Isotope Laboratories), 60 mg/L α-ketobutyric acid (CDLM-7318; Cambridge Isotope Laboratories), and 100 mg/L α-ketoisovaleric acid (CDLM-7317; Cambridge Isotope Laboratories) 1 h before IPTG induction at OD_{600} ∼ 0.8. To express the [U-^{15}N, ^{13}C]-labeled $\alpha\beta$ subdomain (residues 317−505) of $YME1L_{AAA}$, cells were grown in M9 minimal media with $^{15}NH_4Cl$ as the sole nitrogen source and D-glucose-$^{13}C_6$ as the sole carbon source. Protein expression was induced at OD_{600} ∼ 0.8 and then carried out at 25 °C for *ca.* 16 h.

Cells were harvested and resuspended in Ni-A buffer [50 mM Tris, pH 7.4, 500 mM NaCl, 50 mM imidazole], followed by lysis via sonication (45% amplitude, 15 min per sample with 2 s-on/ 2 s-off pulses). The lysed cells were centrifuged at 14,000 × g for 20 min, and the supernatant was subjected to 5 mL of HisPur Ni-NTA Resin (Thermo Scientific). The Ni-NTA Resin column was equilibrated with Ni-A buffer before sample loading, and the bound protein was washed with the Ni-A buffer before elution with Ni−B buffer [25 mM Tris-HCl, pH 7.8, 300 mM imidazole]. The eluted protein was then dialyzed overnight at 4 °C in a buffer containing 50 mM Tris (pH 7.4), 200 mM NaCl, 1 mM DTT, and ubiquitin-like protease (ULP) to remove the His_6-SUMO tag. The protein was then concentrated and purified by a Superdex 200 or 75 Increase 10/300 column (Cytiva) in a buffer containing 50 mM HEPES (pH 7.5) and 100 mM NaCl. For the monomeric YME1L constructs, an additional Ni-NTA purification step was used after ULP cleavage to remove the cleaved His_6-SUMO tag and ULP before the size exclusion chromatography purification step. The purities of all protein preparations was confirmed by SDS-PAGE, and the concentrations were measured using absorbance at 280 nm with extinction coefficients predicted from the primary sequences of the constructs using the Expasy ProtParam tool.

The nucleotide-free state of the YME1L constructs was achieved via apyrase digestion. 5 μL of 500 U/ml apyrase (New England BioLabs) was added to the purified YME1L construct in a buffer containing 50 mM HEPES (pH 7.5), 100 mM NaCl, 1 mM EDTA, and 5 mM $CaCl_2$, and the mixture was incubated overnight at 21 °C. The apyrase-digested sample was purified with a Superdex 200 Increase 10/300 column (Cytiva) in a buffer containing 50 mM HEPES (pH 7.5), 100 mM NaCl, and 1 mM EDTA. The fractions of pure protein were collected, flash frozen in liquid nitrogen, and stored at −80 °C.

Size-Exclusion Chromatography

To characterize the YME1L constructs in the presence of ATP using size-exclusion chromatography (SEC), 30 μM of purified $^{\Delta N}YME1L_{E439Q}$ and $^{hex}YME1L_{E439A}$ were first incubated in a buffer containing 50 mM HEPES (pH 7.5), 100 mM NaCl, 2 mM ATP, 5 mM $MgCl_2$, and 1 mM EDTA for 2 h prior to SEC runs. A total volume of 0.3 mL of protein samples was then injected onto a Superdex 200 Increase 10/300 column (Cytiva) equilibrated with a buffer containing 50 mM HEPES (pH 7.5), 100 mM NaCl, 1 mM EDTA, 2 mM ATP, and 5 mM $MgCl_2$.

Dynamic Light Scattering

Purified $^{hex}YME1L_{E439A}$ was stored in the apo form. For the ATP-bound samples, 10 mM ATP was added to the protein solution prior to the DLS experiments. DLS measurements were performed on a DynaPro DLS Plate Reader III (Wyatt Technology) in a buffer containing 50 mM HEPES (pH 7.5), 100 mM NaCl, 1 mM EDTA, and 15 mM $MgCl_2$. Samples were centrifuged at 20,000 × g at 4 °C for 30 min to eliminate precipitates or solid impurities prior to loading on a 384-well plate. A total of 20 μL of protein sample was loaded to each well, and the plate was centrifuged at 3,000 × g at 4 °C for 5 min to remove air bubbles present in the wells. 10 μL of mineral oil was then added on top of each sample to prevent evaporation, and the plate was centrifuged again at 3,000 × g at 4 °C for 3 min. For each well, 20 measurements with 4.8 s acquisitions were performed, and an average was calculated from the autocorrelation functions. Temperature scans were performed from 7.5 to 50 °C with a step size of 2.5 °C. The

https://doi.org/10.1021/acs.biochem.5c00535
Biochemistry XXXX, XXX, XXX−XXX

autocorrelation functions were fitted using the following equation:

$$g^2(\tau) = B + \beta e^{2\Gamma\tau}\left(1 + \frac{\mu_2}{2}\tau^2\right) \quad (1)$$

where B represents a term accounting for the baseline, β is the correlation function amplitude at τ =0, $\Gamma = Dq^2$, and μ_2 is the second moment of the distribution of Γ values about their mean.[27,28] For the calculation of Γ, D is the translational diffusion coefficient and q is the scattering wave vector calculated by $q = \frac{4\pi n}{\lambda_0}\sin\left(\frac{\theta}{2}\right)$, where n is the solvent refractive index (n = 1.3347), λ_0 is the wavelength of the light used by the instrument, and θ is the scattering angle. D, β, B, and μ_2 were output as fitted parameters, respectively. The hydrodynamic radius, R_h, was converted from the fitted diffusion coefficient, D, using the Stokes−Einstein equation

$$R_h = \frac{k_B T}{6\pi\eta D} \quad (2)$$

where k_B is the Boltzmann constant, T is the temperature in Kelvin, and η is the viscosity.[29]

To estimate the affinity of monomeric $^{\Delta N}$YME1L, DLS measurements were performed at subunit concentrations of 25, 50, 100, 150, and 200 μM at 15 °C. The following model was used to describe the oligomerization process:

$$M + M \rightleftharpoons M_2$$

$$M_2 + M \rightleftharpoons M_3$$

$$M_3 + M \rightleftharpoons M_4$$

$$M_4 + M \rightleftharpoons M_5$$

$$M_5 + M \rightleftharpoons M_6$$

In this model, the equilibrium concentration of each oligomeric species is given by

$$[M_i] = K[M_{i-1}][M] \quad (3)$$

where K is the microscopic association constant. We assume a uniform K across all association steps, implying no cooperativity. The total concentration of the monomer is given by

$$[M_T] = \sum_{i=1}^{6} i[M_i] \quad (4)$$

Using these equations, we can determine $[M_i]$ as a function of $[M_T]$ and K. Meanwhile, the relationship between the hydrodynamic radius, R_h, and molar mass, M, is described by $R_h = a_0 M^{1/\alpha}$, where α typically ranges from 2 to 3 for globular proteins.[30−33] Thus, the hydrodynamic radius of an i-mer follows

$$r_i = r_1 \times i^{1/\alpha} \quad (5)$$

where r_1 is the monomer's hydrodynamic radius and i is the number of monomers in the species. For the DLS measurements, a cumulant analysis of the autocorrelation function was performed to determine the average translational diffusion coefficient, D_{ave}, which was then converted into an average hydrodynamic radius, R_{ave}, using the Stokes−Einstein equation. For a mixture of species, the average hydrodynamic radius, R_{ave}, is given by

$$R_{ave} = \frac{\sum_{i=1}^{6} M_i^2 c_i}{\sum_{i=1}^{6} M_i^2 c_i / r_i} \quad (6)$$

where M_i, c_i, and r_i are the molar mass, the molar concentration, and the hydrodynamic radius of the i-mer. Using eqs 1−6, the experimental R_{ave} values of $^{\Delta N}$YME1L in both the presence and absence of ATP were fitted as a function of protein concentration to extract the association constants K for the nucleotide-free and ATP-bound states, respectively, with α fitted as a global parameter. A grid search was performed, which yielded the best-fit values of α being 2.06 and K being $(3.38 \pm 0.07) \times 10^3$ M^{-1} and $(3.52 \pm 0.07) \times 10^3$ M^{-1} for the ATP-bound and ATP-free states, respectively.

NADH-Coupled ATPase Assay

NADH-coupled ATPase assays[34] were carried out at 25 °C in a reaction buffer containing 25 mM HEPES (pH 7.5), 5 mM $MgCl_2$, 100 mM NaCl, 257 μM NADH, 50 U/ml LDH, and an ATP regeneration system (2 mM ATP, 1 mM PEP, and 20 U/mL PK). A total reaction volume of 100 μL was used with 1.8 μM (hexamer concentration) of the YME1L construct in each reaction. To measure the ATP hydrolysis rate in the presence of Zn^{2+}, a final concentration of 25 μM $ZnCl_2$ was included in the reaction. Reactions were carried out in triplicates. The decrease in absorbance at 340 nm was monitored in a 96-well plate using an Epoch 2 Microplate Spectrophotometer (BioTek Instruments). The ATPase hydrolysis rate was calculated by using Beer's law and the NADH extinction coefficient at 340 nm (ε_{340} = 6,220 $M^{-1}cm^{-1}$).

Protein Degradation Assays

Substrate degradation assays were conducted at 29 °C using 2.6 μM (hexamer concentration) of YME1L in a buffer containing 25 mM HEPES (pH 7.5), 100 mM NaCl, 10 mM $MgCl_2$, 1 mM DTT, 25 μM $ZnCl_2$, and an ATP regeneration system (5 mM ATP, 2 mM PEP, and 2.5 U mL^{-1} PK). 10 μM a α-casein (Sigma-Aldrich, Catalogue #C6780) was used in the reaction. Aliquots were sampled from the reaction mix at various time points and mixed with a 2× SDS-loading buffer (FroggaBio Inc.) including 2 mM DTT to quench the reaction. Degradation was evaluated by SDS-PAGE to separate the band, followed by Coomassie Brilliant Blue G-250 staining. The SDS-PAGE gels were imaged using the BioRad ChemiDocTsM XRS+ gel documentation system, and the band intensities of α-casein as a function of reaction time were quantified using Image LabTM software (Bio-Rad).

NMR Experiments

All protein samples were buffer exchanged using centrifugal filters (Amicon Ultra, 10 kDa MWCO, Millipore Sigma) into either H_2O NMR buffer [25 mM Bis-tris (pH 6.5), 25 mM NaCl, 1 mM EDTA] or D_2O NMR buffer [25 mM HEPES, pH 7.0 (pD 7.4), 25 mM NaCl, 1 mM EDTA] depending on the NMR experiment. The protein samples were centrifuged at 6,000 × g for 1 min to remove any aggregates prior to NMR experiments. NMR experiments were conducted on Bruker AVANCE III 14.1 T and Bruker AVANCE III HD 18.8 T spectrometers equipped with cryogenically cooled, pulse-field gradient, triple-resonance probes. The NMR spectra collected were processed with NMRPipe[35] and visualized using NMRFAM-SPARKY.[36] The ^{1}H-^{13}C HMQC experiments of [$^{13}CH_3$-ILVM]-labeled $^{\Delta N}$YME1L and YME1L$_{AAA}$ were acquired with an interscan delay of 1.5 s with the carriers positioned at 19 and 0.8 ppm and acquisition times of 21.3 and

https://doi.org/10.1021/acs.biochem.5c00535
Biochemistry XXXX, XXX, XXX−XXX

64 ms at the t_1 and t_2 dimensions, respectively. To obtain assignment of the methyl groups, the ^{1}H-^{13}C CT-HSQC experiment of [U-^{15}N, ^{13}C]-labeled $\alpha\beta$ subdomain of $YME1L_{AAA}$was acquired with an interscan delay of 1.5 s with the carriers positioned at 20 and 4.683 ppm and acquisition times of 27.8 and 64 ms at the t_1 and t_2 dimensions, respectively. Two methyl-TROSY-based 3D NOE experiments, which record chemical shifts as ^{13}C[i]-NOE-^{13}C[j]-^{1}H-[j] and ^{1}H[i]-NOE-^{13}C[j]-^{1}H[j],[37,38] respectively, were acquired on [$^{13}CH_3$-ILVM]-labeled $YME1L_{AAA}$ using an NOE mixing time of 200 ms at 18.8 T and 20 °C.

In order to measure the binding affinity of ADP to the monomeric $YME1L_{AAA}$, a titration was performed in which ADP was added to a solution of [$^{13}CH_3$-ILVM]-labeled $YME1L_{AAA}$ (maintained at 100 μM) in a series of 13 steps from 0 to 392 μM. Assuming a one-site binding model, the binding curves were individually fit to the following equation using nonlinear least-square fit:

$$I_{\text{bound}} = I'_{\text{bound}} \times \frac{P_T + L_T + K_d - \sqrt{(P_T + L_T + K_d)^2 - 4P_T L_T}}{2P_T}$$

where I_{bound} is the intensity of the bound peak at each titration point, I'_{bound} is the intensity of the bound peak at the fully bound state, and P_T and L_T are the total concentrations of $YME1L_{AAA}$ and ADP, respectively. Fitting was performed using an in-house Python script employing the "lmfit" package, with K_d and I'_{bound} being the fitted parameters. The final K_d is the average of the individually fitted K_d values with uncertainty obtained from the standard deviation.

HDX-MS

To prepare the samples for the HDX-MS experiments, protein stocks were diluted in an equilibration buffer in H_2O containing 50 mM HEPES (pH 7.5), 100 mM NaCl, 1 mM EDTA, and 10 mM $MgCl_2$. The buffers were supplemented with 10 mM ATP or ADP to create the ATP-bound and ADP-bound states, respectively. For the (ATP, Zn^{2+})-bound ^{hex}YME1L, the protein was incubated in 50 mM HEPES (pH 7.5), 100 mM NaCl, 10 mM $MgCl_2$, 10 mM ATP and 1 mM of $ZnCl_2$. HDX reaction was initiated by a 10-fold dilution into a D_2O-based buffer with the same composition as the equilibration buffer and additives depending on the condition of interest at pD 7.5.[39] HDX reactions were quenched at fixed time points of 0.167, 0.5, 2, 10, and 30 min after the exchange process via acidification to pH of 2.5 in a 1:1 ratio of HDX reaction and quench buffer (250 mM Na_3PO_4, 3 M Gdn-HCl, 3 mM MAPCHO-12, pH 1.37), followed by flash freezing in liquid N_2. The final sample contained 0.033 μM (hexamer concentration) YME1L with a D_2O concentration of ~90%. Samples were stored at −80 °C until LC-MS analysis. All time points and conditions were run in triplicate to assess the reproducibility of the measurements.

For LC-MS, the samples were rapidly thawed and injected into the 50 μL loop of an M-class ACQUITY ultraperformance liquid chromatography (UPLC) equipped with HDX technology (Waters). The protein was digested into smaller peptide fragments via an immobilized Nepenthesin II column (AP-PC-004m, 1 mm × 20 mm, 16.2 μL vol., AffiPro). The generated peptic peptides were trapped on a C18 Vanguard BEH column (ACQUITY UPLC BEH, 1.7 μM, 2.1 mm × 5 mm, Waters) for 3 min at 100 μL min^{-1} prior to MS analysis. While maintaining 0 °C, the trapped peptides were subsequently separated on a UPLC HSS T3 column (ACQUITY, 1.8 μM, 1 mm × 50 mm, Waters) at a 100 μL min^{-1} rate with an 8 min water/acetonitrile gradient acidified with 0.1% formic acid. To minimize the carryover of samples, the trapping and analytical columns were cleaned for 12 extra minutes. Additionally, a pepsin wash (1.5 M Gdn-HCl, 5% acetonitrile, 0.8% formic acid, 1.5 mM MAPCHO-12) was injected 5 times during each run. The LC eluent was directed to a Synapt G2Si mass spectrometer (Waters) equipped with a dual electrospray ionization source (ESI) operated in positive-ion mode. The mass spectrometer fitted with a standard ESI was operated in positive ion mode with a capillary voltage of +3 kV. The instrument was calibrated online via infusion of LeuEnk solution (1+, 556.2771 m/z) from the LockSpray exact mass ionization source (Waters) every 20 s at a flow rate of 10 μL min^{-1}. The cone and desolvation gas flows were set to 90 and 600 L h^{-1}, respectively. The source and desolvation temperatures were 80 and 175 °C, respectively. The instrument was operated in resolution mode with an acquisition m/z range of 50 to 2000 Th. Subsequently, HDX data analysis to measure deuterium uptake was performed using DynamX 3.0 software (Waters).

Peptide mapping was performed in triplicate on undeuterated samples using data-independent acquisition (DIA), also known as the MS^E mode. The MS^E data sets were processed by the ProteinLynx Global Server (PLGS) software program (Waters) searching against a database of the YME1L construct sequence. Additionally, the PLGS processing parameters were set to lock a mass window of 0.4 Da and low energy and elevated energy thresholds of 100 and 50 counts, respectively. PLGS generated ion accounting files in CSV format, consisting of a list of all identified peptides for all three runs of the undeuterated control samples. Information including individual peptide sequences, the number of matched product ions, the charge number, m/z value of all precursor ions was provided from the ion accounting files. Subsequently, YME1L peptides that were identified in all triplicates after filtering using the parameters suggested by Sørensen and colleagues were included to be processed further.[40]

The identified peptides from PLGS were subsequently analyzed using DynamX 3.0 software. The mass spectra of all the peptides under each exchange time point were manually checked to maximize the analysis quality and overall sequence coverage. The deuterium uptake profiles plotting the deuterium uptake of individual exposure points in all states for individual peptides were generated once the mass spectra were fully analyzed. The centroid mass of both deuterated and undeuterated peptide isotope distribution under each time point was obtained according to this equation:

$$\frac{\sum_i \left(\frac{m}{z}\right)_i \times I_i}{\sum_i I_i}$$

where the spectral intensity of the i^{th} channel in the spectrum is represented by I_i.[41] The deuterium uptake differences between conditions were calculated by comparing the centroids of isotope distributions between the deuterated and undeuterated samples. We used a hybrid significance test model that selected peptides with deuterium uptake differences greater than ± 0.5 Da and that also passed Welch's t test with $\alpha < 0.01$,[42] to ascertain significant differences in deuterium uptake. The heat maps were generated using HDgraphiX.[43] All deuterium

https://doi.org/10.1021/acs.biochem.5c00535
Biochemistry XXXX, XXX, XXX−XXX

uptake data, peptide coverage maps, and a summary of experimental conditions (Table S1) are available in the Supporting Information.[44]

DTNB Assay

A Walker-B variant (E439A) was also introduced into the three cysteine variants (M500C, M701C, and M452C) to prevent ATP hydrolysis during the assay. Prior to the DTNB assay, the cysteine variants were incubated with 10 mM DTT to reduce the cysteine followed by size exclusion chromatography to remove DTT from the protein stock solution. 10 mM DTNB was prepared in a buffer containing 100 mM sodium phosphate (pH 7.8) and then diluted to 1 mM in a buffer containing 50 mM HEPES (pH 7.5), 100 mM NaCl, and 1 mM EDTA. A titration was performed by adding 10 μL of protein (80−200 μM monomeric concentration) consecutively to the 1 mM DTNB solution and monitoring the reaction using UV−vis absorbance. For the ATP-bound state, a final concentration of 5 mM ATP and 10 mM $MgCl_2$ was included in both the DTNB and the protein solution prior to the titration. The absorbance at 412 nm was plotted as a function of protein concentration and fitted with a linear function ($y = kx$), in which the slope was used to extract the fraction of reacted thiol groups using an extinction coefficient of 14150 cm^{-1} M^{-1} for TNB.[45]

RESULTS

A Hexamerization Tag Promotes the Formation of Active Hexameric YME1L Catalytic Domain

YME1L must assemble into a hexamer for both its ATPase activity and its ATP-dependent proteolytic function. YME1L oligomerization, in turn, is facilitated by its N-terminal domain (NTD) and transmembrane domain (TMD) (Figure 1A).[6] Glynn and coworkers showed that replacing the NTD and TMD with a soluble 32-residue hexameric coiled-coil domain promotes the hexamerization of the YME1L catalytic domain ($^{\Delta N}$YME1L) and restores its ATPase and protease activities.[6,8] Following this approach, we used the same construct consisting of an N-terminal hex-tag connected to the catalytic domain of YME1L by a 10-residue linker (^{hex}YME1L) (Figure 1A) and characterized its hydrodynamic properties and enzymatic activity.

We first used size exclusion chromatography (SEC) to characterize the oligomeric states of ^{hex}YME1L and $^{\Delta N}$YME1L. The SEC peak of ^{hex}YME1L is centered at 11 mL, while that of $^{\Delta N}$YME1L is at 15 mL (Figure 1C). These elution volumes are consistent with the molecular weights of the hexameric (332 kDa) and monomeric YME1L (51 kDa), respectively, and with previous findings.[6] The elution volume of $^{\Delta N}$YME1L remained unchanged (i.e., monomeric) in the presence of 5 mM ATP (Figure 1C), suggesting that the addition of nucleotide alone is insufficient to promote hexamerization of the catalytic domain in the absence of the hex-tag at low protein concentrations (~6 μM monomeric YME1L concentration at the center of the SEC peak). We subsequently used dynamic light scattering (DLS) to probe the concentration- and temperature-dependence of oligomerization for our YME1L constructs. We measured the hydrodynamic radius of $^{\Delta N}$YME1L and ^{hex}YME1L in the presence and absence of 10 mM ATP at a monomeric concentration of 200 μM (all YME1L concentrations reported hereafter refer to subunit concentrations) (Figure 1D). The difference in hydrodynamic radius between $^{\Delta N}$YME1L and ^{hex}YME1L indicates that $^{\Delta N}$YME1L remains predominantly monomeric even at a [YME1L] of 200 μM, suggesting a low intrinsic propensity for oligomerization. No significant difference in the hydrodynamic radius was observed between the nucleotide-free and ATP-bound states of $^{\Delta N}$YME1L, consistent with the SEC results. To further quantify the self-association affinity of $^{\Delta N}$YME1L, we measured the hydrodynamic radius of $^{\Delta N}$YME1L across a concentration range of 25 to 200 μM (Figure 1E). Fitting these data to an oligomerization model yielded a single-step association constant of $(3.52 \pm 0.07) \times 10^3$ and $(3.38 \pm 0.07) \times 10^3$ M^{-1} for the nucleotide-free and ATP-bound states, respectively (see Materials and Methods), further supporting a low affinity for oligomerization. Additionally, we performed DLS measurements on $^{\Delta N}$YME1L across temperatures ranging from 7.5 to 50 °C (Figure S1). Prior to the onset of protein aggregation, no significant changes in hydrodynamic radius were observed (Figure S1). Collectively, these findings suggest that the catalytic domain of YME1L has a low intrinsic propensity to oligomerize, even in the presence of nucleotide. This observation highlights the crucial role that the N-terminal and transmembrane domains play in facilitating YME1L hexamer formation.

We measured the ATPase activity of our constructs using an NADH-coupled assay.[34] The initial ATPase rate for ^{hex}YME1L was 1.97 ± 0.04 min^{-1} $hexamer^{-1}$ (Figure 1F), consistent with a previous report.[6] In contrast, substituting Walker-B motif E439 for alanine (^{hex}YME1L$_{E439A}$) leads to a 46% reduction in ATPase activity compared to that of ^{hex}YME1L (Figure 1F), in agreement with a conserved mechanism for ATP hydrolysis in AAA+ motors. In addition, the hex-tag together with the AAA+ domain of YME1L (^{hex}YME1L$_{AAA}$) displays ~26% higher ATPase activity compared with ^{hex}YME1L (Figure 1F), suggesting that the AAA+ domain itself is sufficient to form the obligate hexamer to support ATP hydrolysis in the presence of the hex-tag. The AAA+ domain without the hex-tag (YME1L$_{AAA}$) showed no measurable ATPase activity, likely due to the monomeric state of the AAA+ domain (Figure 1F). We also characterized the protease activity of ^{hex}YME1L using α-casein as a model substrate. ^{hex}YME1L degrades α-casein in an ATP-dependent manner (Figure 1G and H, and Figure S2). In contrast, a YME1L variant with a catalytically deficient protease active site (^{hex}YME1L$_{E600Q}$), in which the glutamate in the HEXXH Zn^{2+}-binding motif is substituted with a glutamine,[46,47] showed no protease activity in the presence of ATP (Figure 1G and H, and Figure S2). Furthermore, we observed no appreciable degradation of α-casein by the Walker-B variant (^{hex}YME1L$_{E439A}$) (Figure 1G and H, and Figure S2). These results demonstrate that the hex-tag effectively mimics the hexamerization function of NTD and TMD, thereby enabling the ^{hex}YME1L construct to perform ATP-dependent substrate translocation and degradation.

Nucleotide Binds to the Monomeric AAA+ Domain of YME1L and Modifies Side Chain Dynamics of the AAA+ Domain

We employed solution NMR spectroscopy to examine the effect of nucleotide binding on the side-chain dynamics of YME1L. Given the large molecular weight of YME1L (51 kDa for monomeric $^{\Delta N}$YME1L and 330 kDa for ^{hex}YME1L), we isotopically labeled the methyl groups of Ile (δ1), Leu (δ1,δ2), Val (γ1,γ2), and Met (ε) side chains to introduce NMR-detectable $^{13}CH_3$-methyls in an otherwise highly deuterated

https://doi.org/10.1021/acs.biochem.5c00535
Biochemistry XXXX, XXX, XXX−XXX

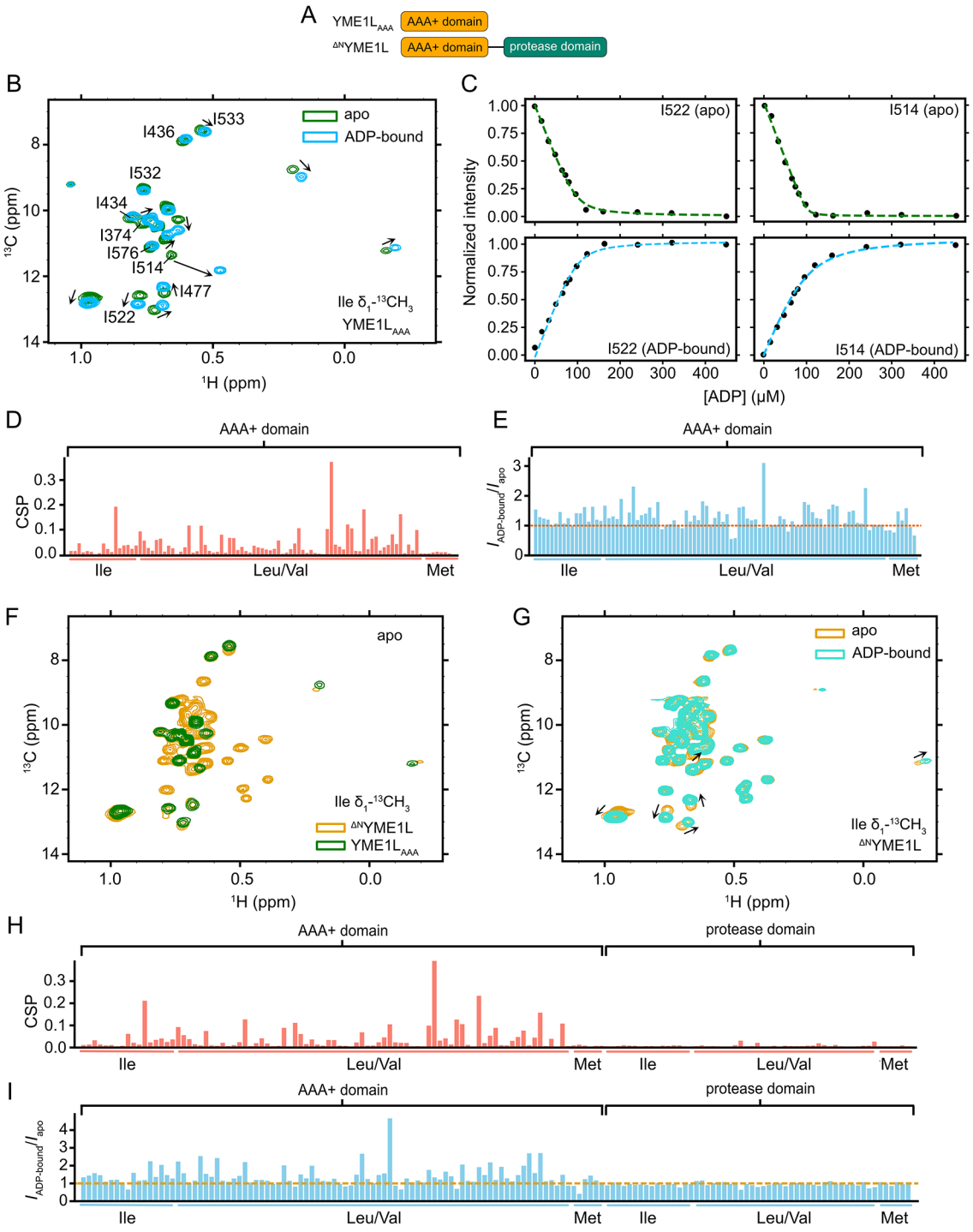

Figure 2. Nucleotide binding alters side chain dynamics in the AAA+ domain. (A) Domain organization of the two constructs, YME1L$_{AAA}$ and $^{\Delta N}$YME1L, presented in the figure. (B) Overlay of ^{1}H-^{13}C HMQC spectra of [U-^{2}H, ILVM-^{13}CH$_3$] labeled YME1L$_{AAA}$ in the presence (blue) and absence (green) of 5 mM ADP. (C) Titration profiles of selected peaks from (B) with increasing concentrations of ADP, fitted to a one-to-one binding model for slow chemical exchange. Chemical shift perturbations (CSPs) (D) and intensity ratios (E) of the methyl peaks in YME1L$_{AAA}$ in the ADP-bound versus apo states. The orange dashed line in (E) indicates an intensity ratio of 1.0. (F) Overlay of ^{1}H-^{13}C HMQC spectra of [U-^{2}H, ILVM-^{13}CH$_3$] labeled YME1L$_{AAA}$ (green) and $^{\Delta N}$YME1L (yellow), respectively, in the apo state. (G) Overlay of ^{13}C-^{1}H HMQC spectra of [U-^{2}H, ILVM-^{13}CH$_3$] labeled $^{\Delta N}$YME1L in the presence (cyan) and absence (yellow) of 5 mM ADP. Chemical shift perturbations (CSPs) (H) and intensity ratios (I) of the methyl peaks in $^{\Delta N}$YME1L in the ADP-bound versus apo states. Spectra were acquired at 14.1 T and 20 °C.

background. This labeling scheme, referred to in what follows as [^{13}CH$_3$-ILVM], in combination with NMR experiments that exploit the methyl-TROSY effect[48−50] allowed us to achieve great sensitivity and resolution in the ^{1}H-^{13}C correlated NMR spectra of the monomeric YME1L$_{AAA}$ (Figure 2B and Figure S3B) and the monomeric $^{\Delta N}$YME1L (Figure 2F and Figure S3C). However, [^{13}CH$_3$-ILVM]-labeled ^{hex}YME1L$_{AAA}$ failed to yield high-quality NMR spectra, potentially due to dynamic oligomerization and structural heterogeneity among subunits (Figure S4A). The spectral quality somewhat improves upon

https://doi.org/10.1021/acs.biochem.5c00535
Biochemistry XXXX, XXX, XXX−XXX

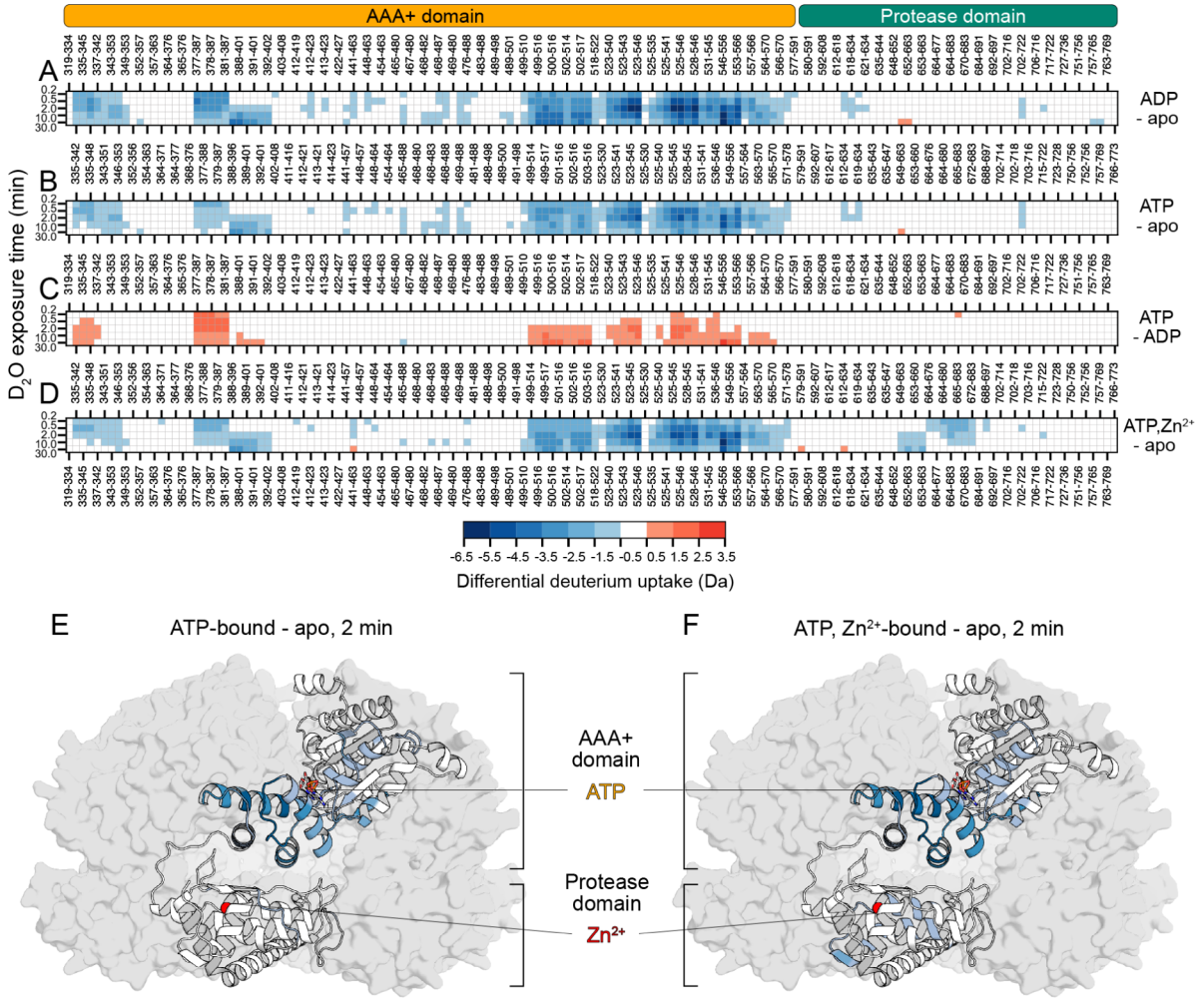

Figure 3. The structural dynamics of ^{hex}YME1L are impacted by the binding of nucleotides. Heatmaps display the differential deuterium uptake of ^{hex}YME1L bound to (A) ADP and (B) ATP relative to apo ^{hex}YME1L. Rigidification is observed across the AAA+ domain, mainly pronounced in regions that line the nucleotide binding site. (C) The deuterium uptake of the ATP-bound state compared to ADP-bound ^{hex}YME1L suggests that the nucleotide binding site is more dynamic when bound to ATP and rigidifies upon hydrolysis. (D) The differential deuterium uptake of ATP- and Zn^{2+}-bound ^{hex}YME1L relative to apo ^{hex}YME1L shows a reduction of deuterium uptake in the nucleotide binding site of the AAA+ domain and the Zn^{2+} binding site of the protease domain. (E) The differential deuterium uptake of ATP-bound relative to apo ^{hex}YME1L after 2 min of deuterium exposure is mapped onto an AlphaFold3[15] structural model of the protein, emphasizing the reduction of deuterium uptake localized in the nucleotide binding site of the AAA+ domain. (F) Upon the addition of Zn^{2+}, rigidification is observed in residues that line the Zn^{2+} binding site in the protease domain. Regions of the protein that are not covered during HDX-MS are shown in gray on the cartoon representation of a monomer.

the addition of a slowly hydrolyzing ATP analogue, ATPγS (Figure S4B), yet the resolution is not sufficient for further NMR-based investigation. Therefore, our NMR characterization focuses on the monomeric YME1L constructs—YME1L$_{AAA}$ and $^{\Delta N}$YME1L. By analyzing the nuclear Overhauser effect (NOE) between methyl groups in YME1L$_{AAA}$, aided by the AlphaFold3-predicted structure of YME1L$_{AAA}$ (Figure S5) and by regional information on the methyl groups obtained from dividing YME1L$_{AAA}$ into two subdomains (Figure S6), we were able obtain unambiguous assignments for 9 of 17 Ile residues in YME1L$_{AAA}$ (Figure 2B). We then characterize the binding of ADP and its effect on the dynamics of the methyl side chains in our monomeric YME1L constructs. We titrated ADP into [$^{13}CH_3$−ILVM]-labeled YME1L$_{AAA}$, which resulted in the appearance of two sets of peaks, corresponding to the ligand-free and ligand-bound populations (Figure S7A). This observation indicates that ADP binds to the monomeric AAA domain and that the binding causes the so-called "slow chemical exchange" process,[51,52] with an exchange rate (k_{ex}) estimated from the NMR spectra to be slower than 15 s^{-1}. This phenomenon can be exploited to quantify concentrations of the free and bound forms of protein. By fitting the titration profiles of the free and bound peaks, we determined an average dissociation constant K_d value of 4.6 ± 2.3 μM (Figure 2C and Figure S7B), consistent with previously reported values.[53] Interestingly, 55 out of the 94 resolved methyl groups in the AAA+ domain displayed a more than 20% increase in peak intensity in the ADP-bound state compared to the apo state (Figure 2E), which could arise from reduced chemical exchange broadening, reduction in methyl order parameters, or differences in overall tumbling of the AAA+ domain upon ADP binding. We subsequently recorded the ^{1}H-^{13}C correlated spectra of [$^{13}CH_3$-ILVM]-labeled $^{\Delta N}$YME1L. The spectrum of YME1L$_{AAA}$ largely overlaps with that of $^{\Delta N}$YME1L (Figure 2F and Figure S8), allowing us to distinguish peaks that originate from the AAA+ domain (present in both YME1L$_{AAA}$ and $^{\Delta N}$YME1L spectra) from those that originate from the protease domain (only present in

https://doi.org/10.1021/acs.biochem.5c00535
Biochemistry XXXX, XXX, XXX−XXX

the $^{\Delta N}$YME1L spectra). Addition of ADP to the monomeric $^{\Delta N}$YME1L induced chemical shift changes in peaks originating from the AAA+ domain (Figure 2G), similar to those observed in the monomeric YME1L$_{AAA}$ (Figure 2B), likely resulting from direct interaction with ADP. However, we did not observe significant chemical shift perturbations in peaks originating from the protease domain (Figure 2H and Figure S3). Furthermore, ADP binding primarily led to increased peak intensities in the AAA+ domain, with minimal changes in the protease domain (Figure 2I), indicating that nucleotide binding predominantly affects side-chain dynamics within the AAA+ domain in the monomeric YME1L construct. Together, these results demonstrate that ADP binding selectively modulates side-chain dynamics within the AAA+ domain of monomeric YME1L, though the absence of full residue-specific assignments limits detailed structural interpretation and motivates further investigation.

Backbone Dynamics of YME1L Is Modulated by Nucleotide and Zn^{2+} Binding

We subsequently used hydrogen/deuterium exchange mass spectrometry (HDX-MS) to examine changes in backbone dynamics across various nucleotide-free and nucleotide-bound states. HDX-MS is highly sensitive to molecular motions, as the HDX rate of individual backbone amides is influenced by their solvent exposure and participation in hydrogen bonding networks.[54] Rigid protein segments undergo HDX slowly, while regions that undergo local conformational fluctuations and transient opening of the hydrogen bonds become deuterated faster.[54] HDX-MS is a well-established tool for investigating the conformational dynamics of AAA+ motor proteins through comparative analyses of nucleotide-free and nucleotide-bound states.[55] Regions involved in ligand binding typically show a decrease in deuterium uptake, while allosteric changes in the protein can result in either an increase or a decrease in uptake.[56]

We performed a bottom-up continuous labeling HDX experiment to monitor the structural transitions of hexameric YME1L in the apo, ADP-bound, ATP-bound, and ATP+Zn^{2+}-bound forms. To reduce the rate of ATP hydrolysis during labeling, experiments were carried out on the ^{hex}YME1L$_{E439A}$ construct. Our peptide mapping strategy identified 157 high-quality peptides with quantifiable deuterium uptake levels, corresponding to 91.1% sequence coverage and a redundancy level of 4.24 (Figure S9). The majority of these peptides displayed unimodal symmetric isotopic profiles that gradually incorporate deuterium over time. This is indicative of EX2 behavior, where the HDX rate (k_{HDX}) is significantly slower than local protein motions (k_{cl}). We compared deuterium uptake along YME1L's sequence across different nucleotide-bound states relative to the apo form and presented the results as heat maps (Figure 3, Figure S10, and Figure S11). In both the ADP-bound (Figure 3A) and ATP-bound (Figure 3B) states, a series of peptides in the AAA+ domain showed reduced deuterium uptake, suggesting that nucleotide binding largely increases the backbone rigidity in this domain. This is consistent with our NMR results where modulation of side chain dynamics was predominantly observed in the AAA+ domain in response to nucleotide binding. Peptides surrounding the nucleotide-binding pocket, in particular those containing the Walker-A motif (peptides 377−387, 377−388, 378−387, 379−387, and 381−387), showed significant reduction in deuterium uptake in the ADP- and ATP-bound states, consistent with the function of the conserved K385 in the Walker-A motif coordinating the β-phosphate of nucleotides.[57−59] Additionally, peptides within the small AAA+ subdomain (residues 509−579) showed decreased deuterium uptake upon nucleotide binding, indicative of loss of conformational dynamics. Nucleotide binding in the cleft between the large and small AAA+ subdomains has been shown to induce interdomain rotations,[59,60] which may underlie the observed rigidification. The second region of homology (SRH) also exhibited reduced flexibility in nucleotide-bound states (peptides 468−488), consistent with its function of interacting with the nucleotide from a neighboring subunit (*in trans*).[61] Interestingly, a comparison between ADP- and ATP-bound states revealed that ADP-bound YME1L showed greater protection (reduced deuterium uptake) in the AAA+ domain, suggesting enhanced backbone rigidity upon nucleotide hydrolysis (Figure 3C and Figure S10 and S11). YME1L is a zinc metalloprotease with active site residues H599, H603, and D677 coordinating a Zn^{2+}. Comparing the deuterium uptake of the ATP, the Zn^{2+}-bound state of ^{hex}YME1L to that of apo ^{hex}YME1L also showed significantly reduced deuterium uptake in the Zn^{2+}-binding region (residues 649−683), as anticipated (Figure 3D).

Unlike the ATPase domain, the protease domain exhibits little change in response to nucleotide binding. Interestingly, we observed a modest decrease in deuterium uptake for several peptides spanning residues 612−634 and 702−722 in the protease domain upon ADP or ATP binding (Figure 3A and B, and Figure S12). Residues 612−634 are located at the interface between the AAA+ and protease domains, while residues 702−722 lie at the subunit interface and at the central pore (Figure S13). This observation suggests potential long-range crosstalk between the AAA+ and protease domains or reduced solvent exposure of the central pore in the protease due to structural rearrangement in the AAA+ domain. Notably, the long-range effect of nucleotide binding was absent in the NMR experiments (Figures 2H and I), which we attribute to the use of the monomeric $^{\Delta N}$YME1L construct in NMR versus the hexameric ^{hex}YME1L construct in HDX-MS. To test this hypothesis, we compared the deuterium uptake of the nucleotide-bound and apo states of monomeric $^{\Delta N}$YME1L (Figure S12). Consistent with the HDX-MS results from the hexameric ^{hex}YME1L, nucleotide binding also induces rigidification of the AAA+ domain of monomeric $^{\Delta N}$YME1L (Figure S14A and B). A comparison between ^{hex}YME1L and $^{\Delta N}$YME1L in the ATP-bound state revealed only slight differences, with ^{hex}YME1L showing marginally more protection throughout the entire sequence (Figure S14C), likely due to the hex-tag-promoted oligomerization (Figure 1). Notably, we only detected the rigidification of the protease domain (peptides 612−634 and 702−722) upon nucleotide binding in the ^{hex}YME1L construct (Figure 3A and B) but not in the $^{\Delta N}$YME1L construct (Figure S14A and B). These results establish that hexamerization is required for the long-range effect of nucleotide binding on the protease domain of YME1L.

Functional Allostery between the AAA+ and Protease Domains of YME1L

To explore potential functional allostery between the AAA+ and protease domains, we introduced an E600Q substitution at the protease active site of ^{hex}YME1L to suppress the proteolytic activity and tested the ATPase activity of the enzyme. Notably,

https://doi.org/10.1021/acs.biochem.5c00535
Biochemistry XXXX, XXX, XXX−XXX

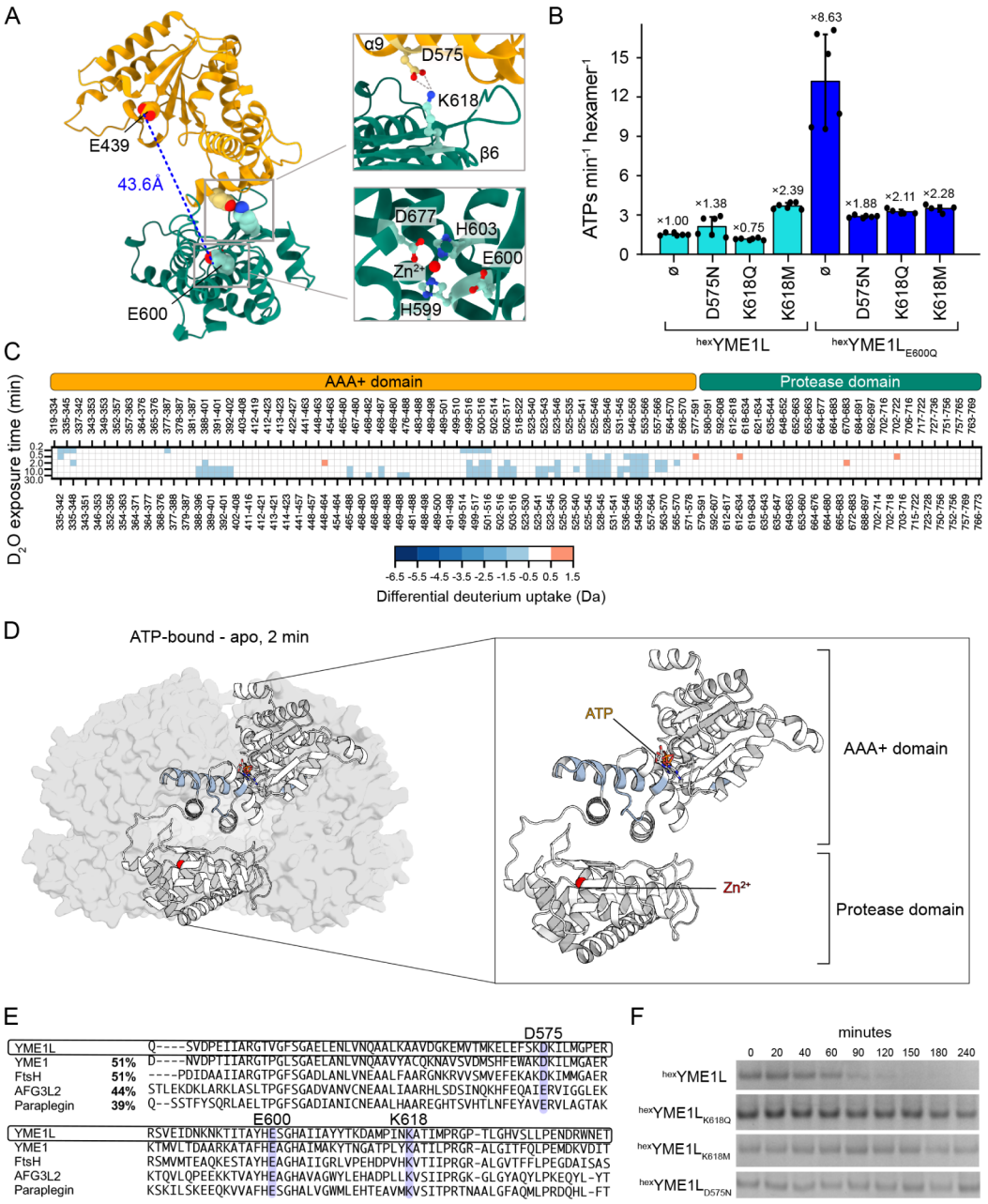

Figure 4. Functional allostery between the AAA+ and protease domains of ^{hex}YME1L. (A) Cartoon representation of the catalytic domain of a YME1L subunit predicted by AlphaFold3,[15] highlighting the distance between E439 (Walker-B motif) at the active site of the AAA+ domain and E600 at the catalytic site of the protease domain (left). The domain interface highlighting residues D575 and K618 that are proposed to form a salt bridge and are involved in allosteric communication between the two domains is enlarged on the upper right. The proteolytic active site is enlarged at the lower right. (B) Rates of ATP hydrolysis of ^{hex}YME1L variants, with D575N, K618Q, and K618M introduced to either ^{hex}YME1L or ^{hex}YME1L$_{E600Q}$. Normalized ATPase activities with respect to those of ^{hex}YME1L are annotated above the bars. (C) Heatmap displays the differential deuterium uptake of ATP-bound ^{hex}YME1L$_{E600Q,E439A}$ relative to apo ^{hex}YME1L$_{E600Q,E439A}$. (D) The differential uptake after 2 min of deuterium exposure is mapped onto a YME1L subunit, highlighting the rigidification observed in the nucleotide binding site of the AAA+ domain. (E) Sequence alignment of YME1L and other homologous AAA+ proteases, including *S. cerevisiae* YME1, *E. coli* FtsH, human AFG3L2, and paraplegin. The overall sequence identity of each homologue to YME1L is shown in percentages. Sequence conservation or similarity for D575, E600Q, and K618 across the homologues is highlighted in blue. (F) SDS-PAGE shows the lack of degradation of α-casein due to the amino acid substitutions that disrupt allostery—K618Q, K618M, and D575N, in comparison with that by ^{hex}YME1L. Images of the uncropped SDS-PAGE gels are shown in Figure S12.

this variant had an 8.6-fold increase in the ATPase activity despite the substitution site being located more than 40 Å from the ATP-binding site (Figure 4A and B). This striking enhancement provides strong evidence for long-range allosteric coupling between the two domains and underscores the structural plasticity of the YME1L complex. In contrast, zinc binding at the protease site had little effect on the ATPase activity (Figure S15), consistent with the HDX-MS data that showed the addition of zinc does not alter the deuterium uptake pattern of the AAA+ domain (Figure 3B and D).

To further investigate the allosteric effect of the E600Q substitution on the conformational dynamics of the AAA+

https://doi.org/10.1021/acs.biochem.5c00535
Biochemistry XXXX, XXX, XXX−XXX

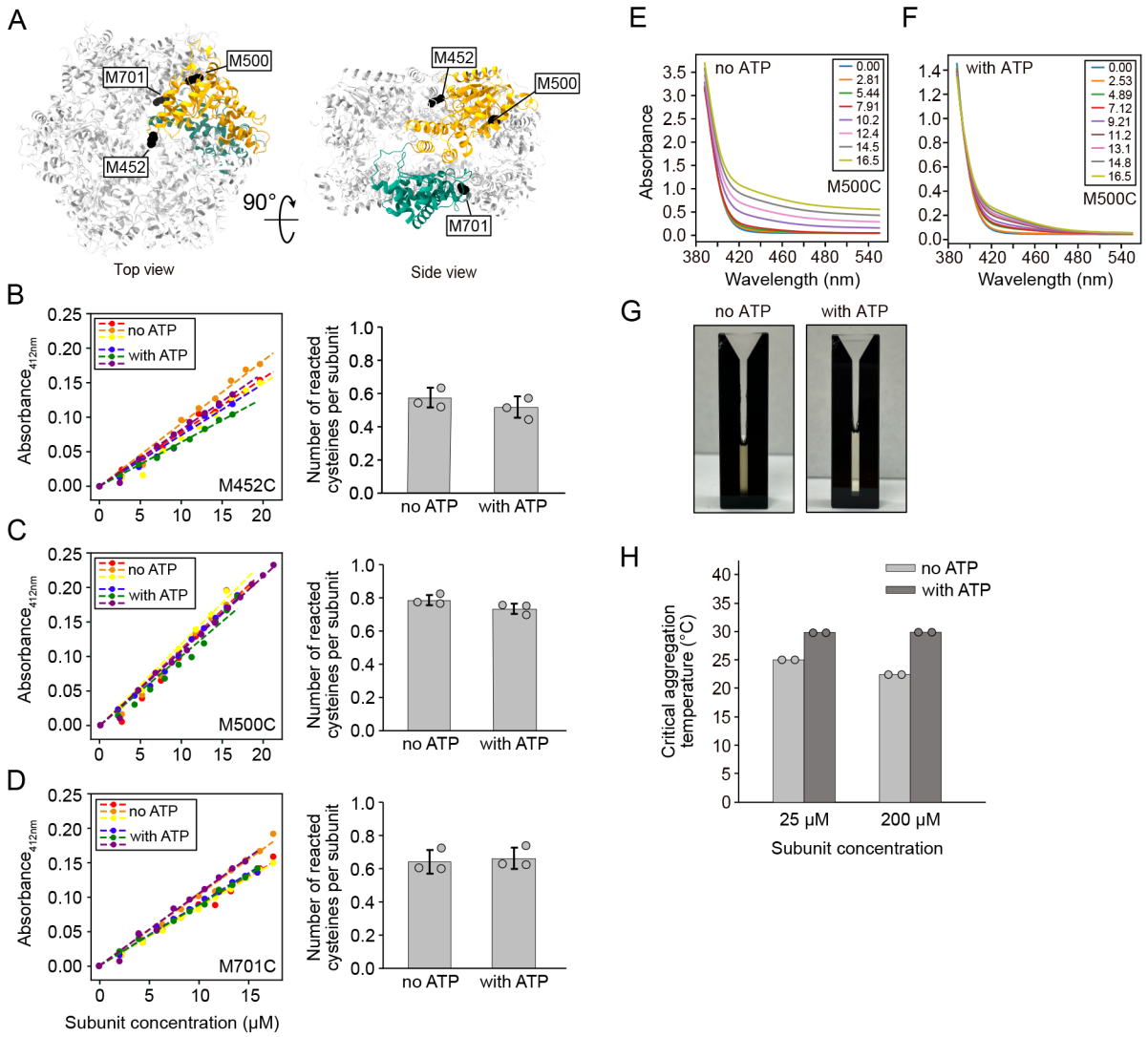

Figure 5. Nucleotide binding increases the stability of YME1L against aggregation. (A) Introduction of three cysteine substitutions in ^{hex}YME1L$_{E439A}$—M452C on the pore-2 loop and M500C and M701C situated at the subunit interface of the AAA+ domain and the protease domain, respectively. (B)−(D) Absorbance changes in the DTNB assay (left) with the number of reacted cysteines per subunit (right) for M452C (B), M500C (C), and M701C (D), in the presence and absence of ATP, recorded at 25 °C. The curves on the left are fitted with a linear correlation $y = ax$. (E, F) Absorbance tracking the titration of M500C into the DTNB solution in the absence (E) and presence (F) of 5 mM ATP. The concentrations of the ^{hex}YME1L subunits are shown in the legend. Aggregation was observed starting at 10.2 μM (subunit concentration) in the absence of ATP, indicated by elevated baselines (E) and turbidity of the solution (G, left), while no aggregation occurred in the presence of ATP (F and G, right). (H) Critical aggregation temperatures of ^{hex}YMEL$_{E439A}$ at subunit concentrations of 25 and 200 μM in the presence and absence of 10 mM ATP, measured by DLS.

domain, we performed HDX-MS experiments on the ^{hex}YME1L$_{E600Q}$ variant in the apo and ATP-bound states (Figure 4C and D). While ATP binding reduced the level of deuterium uptake in the AAA+ domain, as observed in ^{hex}YME1L, the magnitude of the change was substantially diminished in the ^{hex}YME1L$_{E600Q}$ variant (Figure 4C and Figure 2B). This may be as a result of the amino acid substitution shifting the conformational ensemble of the AAA+ domain, reducing the dynamic difference between apo and ATP-bound states, thereby effectively narrowing the energy gap between the resting and transition states and enhancing ATPase activity. Further support for long-range functional coupling comes from the appearance of bimodal isotopic distributions in HDX-MS spectra for residues 354−363 and 388−401, residues involved in nucleotide binding, within both the apo and ATP-bound states of the ^{hex}YME1L$_{E600Q}$ variant (Figure S16). These changes, occurring at sites distant from the E600Q substitution, reinforce the notion of long-range structural communication between AAA+ and protease domains.

To examine this functional crosstalk in more detail, we inspected the interface between the AAA+ and protease domains in the AlphaFold3-predicted structure of YME1L, and we found two residues—D575 (located on α9 in the ATPase domain) and K618 (on β6 in the protease domain)—that are within 3 Å of each other, suggesting a possible salt bridge formation (Figure 4A, upper right). Sequence alignment of YME1L with other homologous AAA+ proteases showed that residues D575 and K618 are conserved (Figure 4E). To test whether this potential salt bridge is essential for allosteric communication, we prepared the D575N, K618Q, and K618M ^{hex}YME1L variants to disrupt the interaction. Notably, none of

https://doi.org/10.1021/acs.biochem.5c00535
Biochemistry XXXX, XXX, XXX−XXX

these point mutations disrupts the assembly of ^{hex}YME1L (Figure S17). Compared to ^{hex}YME1L, these variants alone resulted in only mild effects on the ATPase activity, with the K618Q variant showing a 25% decrease, while the D575N and K618M variants led to 1.38-fold and 2.39-fold increases, respectively (Figure 4B, teal). However, when these substitutions were introduced in the background of the allosterically active ^{hex}YME1L$_{E600Q}$ variant (*i.e.*, ^{hex}YME1L bearing the E600Q & D575N, or E600Q & K618Q, or E600Q & K618M substitutions), the ATP hydrolysis rate decreased by approximately 4-fold in comparison to ^{hex}YME1L$_{E600Q}$ (Figure 4B, blue). This indicates that the allosteric activation of the ATPase activity by E600Q is disrupted by substituting the potential salt bridge at the domain interface, suggesting that the salt bridge plays an important role in the allosteric communication between the AAA+ and protease domains. We then assessed whether this salt bridge is essential in the ATP-dependent protease activity of YME1L by carrying out substrate degradation assays on the D575N, K618Q, and K618M variants of ^{hex}YME1L. Despite that all three variants show comparable or even slightly higher ATPase activity compared to ^{hex}YME1L, none of them is able to degrade the model substrate α-casein (Figures 4F and S18), suggesting the salt bridge between D575 and K618 is crucial for the degradation of protein substrates. These results reveal functional crosstalk between the AAA+ and protease domains of YME1L and the importance of a salt bridge between D575 and K618 in bridging the allosteric communication and in facilitating ATP-dependent substrate degradation.

Nucleotide Binding Increases the Stability of ^{hex}YME1L against Aggregation

We used the DTNB assay to investigate whether nucleotide binding affects the solvent accessibility of the subunit interface and the central channel in ^{hex}YME1L.[62] We selected three residues for substitution with cysteines: (i) M500, located at the subunit interface of the AAA+ domain, (ii) M701, positioned at the subunit interface of the protease domain, and (iii) M452, residing on the pore-2 loop within the central channel (Figure 5A). The naturally occurring C433 in the ^{hex}YME1L construct is not solvent exposed and does not react with DTNB in the assay (Figure S19). All three YME1L cysteine variants assemble into proper hexamers (Figure S20). We titrated the ^{hex}YME1L variants into a solution with excess DTNB and quantified the fraction of reacted cysteines in the absence and presence of 5 mM ATP by measuring the slopes of the absorbance change at 412 nm (Figure 5B−D). The results revealed that 57%, 79%, and 66% of the cysteines reacted with DTNB in the M452C, M500C, and M701C variants, respectively, in the absence of nucleotides, suggesting that all three positions are partially solvent exposed (Figure 5B−D, right). This is consistent with the subunit interface and the central channel experiencing a high degree of local dynamics, consistent with our HDX-MS (Figure 3) and NMR (Figure 2) data. Surprisingly, we observed minimal differences in solvent accessibility across all variants in the presence of ATP (Figure 5B−D). However, increasing concentrations of the TNB-modified ^{hex}YME1L led to protein aggregation, indicated by the elevated baselines in the UV−vis spectra and the apparent turbidity during the assay (Figure 5E and G, left). Intriguingly, the presence of ATP protects the modified ^{hex}YME1L from aggregation at elevated concentrations (Figure 5F and G, right) potentially by stabilizing the conformation of the AAA+ domain.

In addition to the DTNB analysis, we evaluated the thermal stability of ^{hex}YME1L against aggregation by using dynamic light scattering (DLS). By monitoring the autocorrelation profiles of ^{hex}YME1L as a function of temperature, we leveraged the sensitivity of DLS to detect large aggregates (Figure S21).[63] Since aggregation is dependent on protein concentrations, we tested ^{hex}YME1L at subunit concentrations of 25 and 200 μM. The results show that ^{hex}YME1L starts to aggregate when the temperature reaches above 25.0 and 22.5 °C (referred to as the critical aggregation temperature) in the nucleotide-free state at subunit concentrations of 25 and 200 μM, respectively (Figure 5H, Figure S21A andC). The addition of 10 mM ATP, however, increased the thermal stability of ^{hex}YME1L, raising the critical aggregation temperatures by 5 and 7.5 °C at 25 and 200 μM, respectively (Figure 5H and Figure S21B andD). We also observed a similar stabilizing effect of ATP on the monomeric $^{\Delta N}$YME1L construct where ATP binding increases the critical aggregation temperatures of $^{\Delta N}$YME1L at both 25 and 200 μM and protects the protein from thermally induced aggregation (Figure S22). These results demonstrate that ATP binding stabilizes YME1L by reducing its propensity for aggregation and increasing its thermal stability, providing a potential explanation for its ATP-dependent regulation by OMA1 under cellular conditions.[9] However, this model will need to be tested in cell-based systems.

DISCUSSION

Nucleotide binding and hydrolysis are critical components of the functional mechanisms of AAA+ proteins. Oligomerization of the AAA+ domains, often induced or stabilized by nucleotide binding, is essential for their functions, typically by facilitating the formation of active sites for ATP hydrolysis at subunit interfaces and the formation of the central channel as the passage of substrates. ATP binding and hydrolysis drive cooperative conformational changes in the subunits, leading to substrate translocation and remodeling.[59,64,65] Interestingly, for YME1L, nucleotide binding also appears to regulate the degradation of the enzyme itself.[23,25,66] Previous studies have demonstrated that ATP-independent mitochondrial protease OMA1 rapidly degrades YME1L in response to acute oxidative stress, with ATP depletion being a prerequisite for its degradation. It has been proposed that ATP binding enhances the conformational stability of YME1L, thereby reducing its susceptibility to proteolytic degradation.[23,66] Furthermore, in vitro proteinase K degradation assays have indicated distinct conformational states for YME1L in the presence and absence of nucleotides.[25] Although the high-resolution structure of substrate-engaged yeast YME1 has been elucidated,[8] the substrate-free conformation of human YME1L (51% homology with yeast YME1) remains unknown. This raises important questions regarding the mechanism by which nucleotide binding prevents YME1L degradation by activated OMA1 following mitochondrial membrane depolarization. In this study, we investigated the effects of nucleotide binding on the conformational dynamics and structural stability of YME1L using several structural and biophysical tools that include HDX-MS, NMR, dynamic light scattering, and side-chain chemical modification assays. Our findings demonstrate that nucleotide binding stabilizes the catalytic domain of YME1L, providing a potential explanation for how nucleotide binding

https://doi.org/10.1021/acs.biochem.5c00535
Biochemistry XXXX, XXX, XXX−XXX

protects YME1L from OMA1-dependent degradation. In the absence of ATP, YME1L may adopt a less stable or more aggregation-prone conformation, making it more susceptible to degradation by OMA1. Conversely, when ATP is bound, the enzyme remains in a more stable folded state, preventing degradation.

Our HDX-MS data reveal that ATP and ADP binding significantly reduce backbone flexibility in the AAA+ domain of YME1L, particularly within the small helical AAA+ subdomain. Notably, these nucleotide-induced changes in backbone dynamics of the AAA+ domain are observed in both hexameric and monomeric YME1L (Figure 3 and Figure S14), suggesting that the rigidification of the AAA+ domain occurs within individual subunits rather than arising from structural rearrangements at subunit interfaces. This observation is consistent with previous structural studies, indicating that the large and small AAA+ subdomains undergo substantial movements relative to each other in a nucleotide-dependent manner. These movements coordinate concerted structural rearrangements among the subunits during substrate translocation.[8] Moreover, our HDX-MS results demonstrate similar deuterium uptake protection patterns for ATP- and ADP-bound states, with the highest protection observed in the ADP-bound state and the lowest in the apo state (Figure 3C and Figure S11). Interestingly, prior structural studies indicate that the two AAA+ subdomains are closest in the ADP-bound state and farthest apart in the apo state, coinciding with their relative backbone dynamics at different nucleotide states.[8] Additionally, reduced deuterium uptake in the Walker-A motif, which is directly involved in nucleotide binding, has also been observed in other AAA+ motors such as HSP104[67] and ClpX.[68] These findings are consistent with earlier reports showing that the binding of nucleotide protects YME1L from hydrogen peroxide-induced conformational changes[25] and prevents its degradation in isolated mitochondria.[23] Moreover, ATP binding also mitigates chemical-modification-induced and thermally induced aggregation of YME1L, further emphasizing its structural stabilizing role.

Unlike many AAA+ proteins, truncated YME1L constructs that lack the N-terminal and transmembrane domains exhibit a low intrinsic propensity for oligomerization. Our DLS measurements across a range of protein concentrations, temperatures, and nucleotide conditions show no evidence of oligomerization for the soluble domain. This contrasts with homologous AAA+ proteases, such as FtsH and AFG3L2, that oligomerize either in the absence or presence of nucleotides.[46,69] The low oligomerization propensity of YME1L may result from a loosely packed or highly dynamic subunit interface, which may result in partial solvent accessibility of the engineered cysteines at the subunit interface, as observed in the DTNB assays. The dynamic organization of the hexameric YME1L is also reflected in the poor quality of the NMR spectrum of [$^{13}CH_3$-ILVM]-labeled $^{hex}YME1L_{AAA}$ (Figure S4A), while improvement of the spectral quality upon the addition of ATPγS suggests that nucleotide binding reduces conformational dynamics and improves conformational homogeneity in the hexamer (Figure S4B). The dynamic nature of the YME1L catalytic domain likely impedes high-resolution structural determination by cryo-EM in the substrate-free state[8] and could correlate with its rapid degradation under oxidative stress at ATP-depleted conditions.[23]

Allostery plays a pivotal role in the functional mechanisms of AAA+ proteins. In most classic clade AAA+ proteins,[70] ATP binding and hydrolysis are allosterically coupled to the motion of pore loops, which facilitates substrate unfolding and/or translocation.[8,59,71,72] Our HDX-MS results reveal reduced deuterium uptake in the pore-2 loop (residues 446−454) upon nucleotide binding, consistent with this conserved translocation mechanism. More interestingly, we observed long-range allosteric communication between the AAA+ and protease domains of YME1L. Amino acid substitution in the protease active site leads to a significant increase in the ATPase activity of the enzyme and alters the conformational dynamics of the AAA+ domain. This allosteric communication appears to be mediated by a conserved salt bridge at the domain interface, as substitutions of the two residues involved in the salt bridge abolish allosteric activation of ATPase function and diminish the proteolytic activity of the enzyme. Long-range allostery, either between different subunits or between the AAA+ and other functional domains, has been reported to play an important role in working mechanisms of AAA+ proteins.[46,71,73−78] For example, in AAA+ Lon protease, allosteric activation of the proteolytic activity has been reported by substrate binding via induction of a "closed" ring conformation in the AAA+ domain.[79] To our knowledge, our results constitute the first observation of a direct coupling between the AAA+ and protease domains in YME1L, contributing to a growing body of evidence that underscores the critical role of interdomain allosteric communication in AAA+ proteins.

CONCLUSION

In conclusion, our study demonstrates that nucleotide binding not only facilitates YME1L's enzymatic functions but also plays a pivotal role in modulating its conformational dynamics and structural stability, potentially contributing to the regulation of its degradation under oxidative stress. Furthermore, the observed allosteric communication between nucleotide hydrolysis and proteolytic activity highlights new opportunities to manipulate the YME1L function through allosteric mechanisms.

ASSOCIATED CONTENT

Data Availability Statement

All processed data are available in the article and Supporting Information. Mass spectrometry data are available from the MassIVE database under entry MSV000096916.

Supporting Information

The Supporting Information is available free of charge at https://pubs.acs.org/doi/10.1021/acs.biochem.5c00535.

Characterization of conformational dynamics and structural plasticity of the catalytic domain of human mitochondrial YME1L protease (Figures S1−S22) (PDF)

Accession Codes

YME1L: Q96TA2.

AUTHOR INFORMATION

Corresponding Authors

Siavash Vahidi − *Department of Molecular and Cellular Biology, University of Guelph, Guelph, Ontario N1G 2W1, Canada;* orcid.org/0000-0001-8637-3710; Email: svahidi@uoguelph.ca

https://doi.org/10.1021/acs.biochem.5c00535
Biochemistry XXXX, XXX, XXX−XXX

Rui Huang − *Department of Chemistry, University of Guelph, Guelph, Ontario N1G 2W1, Canada;* orcid.org/0000-0002-4064-6397; Email: rhuang08@uoguelph.ca

Authors

Megan K. Black − *Department of Chemistry, University of Guelph, Guelph, Ontario N1G 2W1, Canada*

Angelina Kim − *Department of Molecular and Cellular Biology, University of Guelph, Guelph, Ontario N1G 2W1, Canada;* orcid.org/0009-0004-9479-1700

Ching Y. Chen − *Department of Chemistry, University of Guelph, Guelph, Ontario N1G 2W1, Canada*

Monica M. Goncalves − *Department of Molecular and Cellular Biology, University of Guelph, Guelph, Ontario N1G 2W1, Canada*

Simrah Waseem − *Department of Chemistry, University of Guelph, Guelph, Ontario N1G 2W1, Canada*

Complete contact information is available at: https://pubs.acs.org/10.1021/acs.biochem.5c00535

Author Contributions

[#]M.K.B. and A.K. contributed equally to this work. M.K.B., A.K., C.Y.C., M.M.G., S.W., S.V., and R.H.: formal analysis; M.K.B., A.K., C.Y.C., M.M.G., S.W., S.V., and R.H.: investigation; S.V. and R.H.: supervision; M.K.B., A.K., C.Y.C., M.M.G., S.V., and R.H.: visualization; M.K. B., A.K., S.V., and R.H.: writing—original draft; M.K.B., M.M.G., S.V., and R.H.: writing—review and editing; M.K.B., A.K., C.Y.C., M.M.G., S.W., S.V., and R.H.: methodology; S.V. and R.H.: resources; S.V. and R.H.: funding acquisition; S.V. and R.H.: project administration.

Notes

The authors declare no competing financial interest.

■ ACKNOWLEDGMENTS

M.K.B. acknowledges support for an NSERC Canada Graduate Scholarship. C.Y.C. and M.M.G. acknowledge support for the Ontario Graduate Scholarship. Financial support was provided by a Natural Sciences and Engineering Research Council of Canada Discovery Grant (RGPIN-2021-02843) to S.V. and (RGPIN-2020-00527) to R.H. MS data were recorded at the Mass Spectrometry Facility of the Advanced Analysis Centre, University of Guelph. We thank Dr. Dyanne Brewer (University of Guelph) for assistance with MS measurements. NMR data were recorded at the University of Guelph NMR Center. We thank Dr. Sameer Al-Abdul-Wahid (University of Guelph) for support with NMR measurements. The DLS data were recorded in the Structural & Biophysical Core Facility at the Hospital for Sick Children, Toronto. We thank Dr. Robert W. Harkness (University of Guelph) for assistance with the data acquisition. We thank Dr. Algirdas Velyvis for the critical review of the manuscript.

■ ABBREVIATIONS

AAA+, ATPases Associated with diverse cellular Activities
ADP, adenosine diphosphate
ATP, adenosine triphosphate
ATPγS, adenosine 5′-O-(3-thio)triphosphate
DLS, dynamic light scattering
DTNB, 5,5-dithio-bis(2-nitrobenzoic acid)
DTT, dithiothreitol
ESI, electrospray ionization
Gdn-HCl, guanidine hydrochloride
HDX, hydrogen−deuterium exchange
IPTG, isopropyl-β-D-1-thiogalactopyranoside
IMM, inner mitochondrial membrane
IMS, intermembrane space
K_d, equilibrium dissociation constant
LC, liquid chromatography
LDH, lactate dehydrogenase
L-OPA1, long form of OPA1
m/z, mass to charge ratio
MS, mass spectrometry
MWCO, molecular weight cutoff
NMR, nuclear magnetic resonance
NADH, reduced nicotinamide adenine dinucleotides
NTD, N-terminal domain
OD_{600}, optical density
PAGE, polyacrylamide gel electrophoresis
PEP, phosphoenolpyruvate
PK, pyruvate kinase
SDS, sodium dodecyl sulfate
SEC, size exclusion chromatography
S-OPA1, short form of OPA1
SUMO, small ubiquitin-like modifier
TMD, transmembrane domain
TNB, 2-nitro-5-thiobenzoate
TROSY, transverse relaxation optimized spectroscopy
ULP, ubiquitin-like protease
UPLC, ultraperformance liquid chromatography
UV, ultraviolet
Vis, visible

■ REFERENCES

(1) Pagliarini, D. J.; Calvo, S. E.; Chang, B.; Sheth, S. A.; Vafai, S. B.; Ong, S.-E.; Walford, G. A.; Sugiana, C.; Boneh, A.; Chen, W. K.; Hill, D. E.; Vidal, M.; Evans, J. G.; Thorburn, D. R.; Carr, S. A.; Mootha, V. K. A Mitochondrial Protein Compendium Elucidates Complex I Disease Biology. *Cell* **2008**, *134*, 112−123.

(2) Lopez, M. F.; Kristal, B. S.; Chernokalskaya, E.; Lazarev, A.; Shestopalov, A. I.; Bogdanova, A.; Robinson, M. High-throughput profiling of the mitochondrial proteome using affinity fractionation and automation. *Electrophoresis* **2000**, *21*, 3427−3440.

(3) Song, J.; Herrmann, J. M.; Becker, T. Quality control of the mitochondrial proteome. *Nat. Rev. Mol. Cell Biol.* **2021**, *22*, 54−70.

(4) Steele, T. E.; Glynn, S. E. Mitochondrial AAA proteases: A stairway to degradation. *Mitochondrion* **2019**, *49*, 121−127.

(5) Feng, Y.; Nouri, K.; Schimmer, A. D. Mitochondrial ATP-Dependent Proteases—Biological Function and Potential Anti-Cancer Targets. *Cancers* **2021**, *13*, 2020.

(6) Shi, H.; Rampello, A. J.; Glynn, S. E. Engineered AAA+ proteases reveal principles of proteolysis at the mitochondrial inner membrane. *Nat. Commun.* **2016**, *7*, 13301.

(7) Coppola, M.; Pizzigoni, A.; Banfi, S.; Bassi, M. T.; Casari, G.; Incerti, B. Identification and Characterization of YME1L1, a Novel Paraplegin-Related Gene. *Genomics* **2000**, *66*, 48−54.

(8) Puchades, C.; Rampello, A. J.; Shin, M.; Giuliano, C. J.; Wiseman, R. L.; Glynn, S. E.; Lander, G. C. Structure of the mitochondrial inner membrane AAA+ protease YME1 gives insight into substrate processing. *Science* **2017**, *358*, No. eaao0464.

(9) Rainbolt, T. K.; Saunders, J. M.; Wiseman, R. L. YME1L degradation reduces mitochondrial proteolytic capacity during oxidative stress. *EMBO Rep.* **2015**, *16*, 97−106.

(10) Qi, Y.; Liu, H.; Daniels, M. P.; Zhang, G.; Xu, H. Loss of Drosophila i-AAA protease, dYME1L, causes abnormal mitochondria and apoptotic degeneration. *Cell Death Differ.* **2016**, *23*, 291−302.

(11) Abass, S. A.; Abdel-Hamid, N. M.; Elshazly, A. M.; Abdo, W.; Zakaria, S. OMA1 and YME1L as a Diagnostic Panel in Hepatocellular Carcinoma. *Yale J. Biol. Med.* **2023**, *96*, 443−454.
(12) Sun, X.; Shi, C.; Dai, J.; Zhang, M.-Q.; Pei, D.-S.; Yang, L. Targeting the mitochondrial protein YME1L to inhibit osteosarcoma cell growth in vitro and in vivo. *Cell Death Dis.* **2024**, *15*, 346.
(13) Xia, Y.; He, C.; Hu, Z.; Wu, Z.; Hui, Y.; Liu, Y.-Y.; Mu, C.; Zha, J. The mitochondrial protein YME1 Like 1 is important for non-small cell lung cancer cell growth. *Int. J. Biol. Sci.* **2023**, *19*, 1778−1790.
(14) Cheng, F.; Huang, H.; Yin, S.; Liu, J.-S.; Sun, P. Expression and functional implications of YME1L in nasopharyngeal carcinoma. *Cell Death Dis.* **2024**, *15*, 423.
(15) Abramson, J.; Adler, J.; Dunger, J.; Evans, R.; Green, T.; Pritzel, A.; Ronneberger, O.; et al. Accurate structure prediction of biomolecular interactions with AlphaFold 3. *Nature* **2024**, *630*, 493−500.
(16) Stiburek, L.; Cesnekova, J.; Kostkova, O.; Fornuskova, D.; Vinsova, K.; Wenchich, L.; Houstek, J.; Zeman, J. YME1L controls the accumulation of respiratory chain subunits and is required for apoptotic resistance, cristae morphogenesis, and cell proliferation. *Mol. Biol. Cell* **2012**, *23*, 1010−1023.
(17) Macvicar, T.; Ohba, Y.; Nolte, H.; Mayer, F. C.; Tatsuta, T.; Sprenger, H.-G.; Lindner, B.; Zhao, Y.; Li, J.; Bruns, C.; Krüger, M.; Habich, M.; Riemer, J.; Schwarzer, R.; Pasparakis, M.; Henschke, S.; Brüning, J. C.; Zamboni, N.; Langer, T. Lipid signalling drives proteolytic rewiring of mitochondria by YME1L. *Nature* **2019**, *575*, 361−365.
(18) Anand, R.; Wai, T.; Baker, M. J.; Kladt, N.; Schauss, A. C.; Rugarli, E.; Langer, T. The i-AAA protease YME1L and OMA1 cleave OPA1 to balance mitochondrial fusion and fission. *J. Cell Biol.* **2014**, *204*, 919−929.
(19) Del Dotto, V.; Mishra, P.; Vidoni, S.; Fogazza, M.; Maresca, A.; Caporali, L.; Mccaffery, J. M.; Cappelletti, M.; Baruffini, E.; Lenaers, G.; Chan, D.; Rugolo, M.; Carelli, V.; Zanna, C. OPA1 Isoforms in the Hierarchical Organization of Mitochondrial Functions. *Cell Rep.* **2017**, *19*, 2557−2571.
(20) Ban, T.; Ishihara, T.; Kohno, H.; Saita, S.; Ichimura, A.; Maenaka, K.; Oka, T.; Mihara, K.; Ishihara, N. Molecular basis of selective mitochondrial fusion by heterotypic action between OPA1 and cardiolipin. *Nat. Cell Biol.* **2017**, *19*, 856−863.
(21) Zhang, D.; Zhang, Y.; Ma, J.; Zhu, C.; Niu, T.; Chen, W.; Pang, X.; Zhai, Y.; Sun, F. Cryo-EM structures of S-OPA1 reveal its interactions with membrane and changes upon nucleotide binding. *Elife* **2020**, *9*, No. e50294.
(22) Van Der Bliek, A. M.; Shen, Q.; Kawajiri, S. Mechanisms of Mitochondrial Fission and Fusion. *Cold Spring Harb Perspect Biol.* **2013**, *5*, a011072.
(23) Zhang, K.; Li, H.; Song, Z. Membrane depolarization activates the mitochondrial protease OMA1 by stimulating self-cleavage. *EMBO Rep.* **2014**, *15*, 576−585.
(24) Wai, T.; García-Prieto, J.; Baker, M. J.; Merkwirth, C.; Benit, P.; Rustin, P.; Rupérez, F. J.; Barbas, C.; Ibañez, B.; Langer, T. Imbalanced OPA1 processing and mitochondrial fragmentation cause heart failure in mice. *Science* **2015**, *350*, aad0116.
(25) Brambley, C. A.; Marsee, J. D.; Halper, N.; Miller, J. M. Characterization of Mitochondrial YME1L Protease Oxidative Stress-Induced Conformational State. *J. Mol. Biol.* **2019**, *431*, 1250−1266.
(26) Conicella, A. E.; Huang, R.; Ripstein, Z. A.; Nguyen, A.; Wang, E.; Löhr, T.; Schuck, P.; Vendruscolo, M.; Rubinstein, J. L.; Kay, L. E. An intrinsically disordered motif regulates the interaction between the p47 adaptor and the p97 AAA+ ATPase. *Proc. Natl. Acad. Sci. U. S. A.* **2020**, *117*, 26226−26236.
(27) Koppel, D. E. Analysis of macromolecular polydispersity in intensity correlation spectroscopy: The method of cumulants. *J. Chem. Phys.* **1972**, *57*, 4814−4820.
(28) Frisken, B. J. Revisiting the method of cumulants for the analysis of dynamic light-scattering data. *Appl. Opt.* **2001**, *10*, 4087−4091.
(29) Hanlon, A. D.; Larkin, M. I.; Reddick, R. M. Free-Solution, Label-Free Protein-Protein Interactions Characterized by Dynamic Light Scattering. *Biophys. J.* **2010**, *98*, 297−304.
(30) Tanford, C.; Huggins, M. L. Physical Chemistry of Macromolecules. *J. Electrochem. Soc.* **1962**, *109*, 98C.
(31) Van Holde, K. E.; Johnson, W. C.; Ho, P. S. *Principles of physical biochemistry*; Pearson/Prentice Hall: Upper Saddle River, NJ, 2006.
(32) Claes, P.; Dunford, M.; Kenney, A.; Vardy, P.; Harding, S. E.; Satelle, D. B.; Bloomfield, V. A. *An on-line Dynamic light scattering instrument for macromolecular characterization*; Royal Society of Chemistry: Cambridge, 1992.
(33) Sharma, P.; Rajalingam, D.; Kumar, T. K. S.; Singh, S. A Light Scattering Study of the Interaction of Fibroblast Growth Factor (FGF). with its Receptor. *Biophys. J.* **2008**, *94*, L71−L73.
(34) Norby, J. G. Coupled Assay of Na+,K ± ATPase Activity. *Methods Enzymol.* **1988**, *156*, 116−119.
(35) Delaglio, F.; Grzesiek, S.; Vuister, G. W.; Zhu, G.; Pfeifer, J.; Bax, A. NMRPipe: A multidimensional spectral processing system based on UNIX pipes. *J. Biomol. NMR* **1995**, *6*, 277−293.
(36) Lee, W.; Tonelli, M.; Markley, J. L. NMRFAM-SPARKY: Enhanced software for biomolecular NMR spectroscopy. *Bioinformatics* **2015**, *31*, 1325−1327.
(37) Sprangers, R.; Kay, L. E. Quantitative dynamics and binding studies of the 20S proteasome by NMR. *Nature* **2007**, *445*, 618−622.
(38) Zwahlen, C.; Gardner, K. H.; Sarma, S. P.; Horita, D. A.; Byrd, R. A.; Kay, L. E. An NMR Experiment for Measuring Methyl−Methyl NOEs in 13C-Labeled Proteins with High Resolution. *J. Am. Chem. Soc.* **1998**, *120*, 7617−7625.
(39) Krężel, A.; Bal, W. A formula for correlating pKa values determined in D2O and H2O. *J. Inorg. Biochem.* **2004**, *98*, 161−166.
(40) Sørensen, L.; Salbo, R. Optimized Workflow for Selecting Peptides for HDX-MS Data Analyses. *J. Am. Soc. Mass Spectrom.* **2018**, *29*, 2278−2281.
(41) Weis, D. D.; Engen, J. R.; Kass, I. J. Semi-Automated Data Processing of Hydrogen Exchange Mass Spectra Using HX-Express. *J. Am. Soc. Mass Spectrom.* **2006**, *17*, 1700−1703.
(42) Engen, J. R.; Wales, T. E. Analytical Aspects of Hydrogen Exchange Mass Spectrometry. *Annu. Rev. Anal. Chem.* **2015**, *8*, 127−148.
(43) Vosper, K. R.; Velyvis, A.; Vahidi, S. HDgraphiX: A Web-Based Tool for Visualization of Hydrogen/Deuterium Exchange Mass Spectrometry Data. *J. Am. Soc. Mass Spectrom.* **2025**, *36*, 1200−1203.
(44) Masson, G. R.; Burke, J. E.; Ahn, N. G.; Anand, G. S.; Borchers, C.; Brier, S.; Bou-Assaf, G. M.; Engen, J. R.; Englander, S. W.; Faber, J.; Garlish, R.; Griffin, P. R.; Gross, M. L.; Guttman, M.; Hamuro, Y.; Heck, A. J. R.; Houde, D.; Iacob, R. E.; Jørgensen, T. J. D.; Kaltashov, I. A.; Klinman, J. P.; Konermann, L.; Man, P.; Mayne, L.; Pascal, B. D.; Reichmann, D.; Skehel, M.; Snijder, J.; Strutzenberg, T. S.; Underbakke, E. S.; Wagner, C.; Wales, T. E.; Walters, B. T.; Weis, D. D.; Wilson, D. J.; Wintrode, P. L.; Zhang, Z.; Zheng, J.; Schriemer, D. C.; Rand, K. D. Recommendations for performing, interpreting and reporting hydrogen deuterium exchange mass spectrometry (HDX-MS). experiments. *Nat. Methods* **2019**, *16*, 595−602.
(45) Riddles, P. W.; Blakeley, R. L.; Zerner, B. Ellman's Reagent: 5,5′-Dithiobis(2-nitrobenzoic Acid).-a Reexamination. *Anal. Biochem.* **1979**, *94*, 75−81.
(46) Puchades, C.; Ding, B.; Song, A.; Wiseman, R. L.; Lander, G. C.; Glynn, S. E. Unique Structural Features of the Mitochondrial AAA + Protease AFG3L2 Reveal the Molecular Basis for Activity in Health and Disease. *Mol. Cell* **2019**, *75*, 1073−1085.
(47) Li Binz, T.; Binz, H.; Niemann, B. R.; Singh, B. R. Probing the Mechanistic Role of Glutamate Residue in the Zinc-Binding Motif of Type A Botulinum Neurotoxin Light Chain. *Biochemistry* **2000**, *39*, 2399−2405.
(48) Rosenzweig, R.; Kay, L. E. Solution NMR Spectroscopy Provides an Avenue for the Study of Functionally Dynamic Molecular Machines: The Example of Protein Disaggregation. *J. Am. Chem. Soc.* **2016**, *138*, 1466−1477.

https://doi.org/10.1021/acs.biochem.5c00535
Biochemistry XXXX, XXX, XXX−XXX

(49) Tugarinov, V.; Hwang, P. M.; Ollerenshaw, J. E.; Kay, L. E. Cross-correlated relaxation enhanced 1H-13C NMR spectroscopy of methyl groups in very high molecular weight proteins and protein complexes. *J. Am. Chem. Soc.* **2003**, *125*, 10420−10428.
(50) Jiang, Y.; Kalodimos, C. G. NMR Studies of Large Proteins. *J. Mol. Biol.* **2017**, *429*, 2667−2676.
(51) Bain, A. D. Chemical exchange in NMR. *Prog. Nucl. Magn. Reson. Spectrosc.* **2003**, *43*, 63−103.
(52) Palmer, A. G., III; Kroenke, C. D.; Patrick Loria, J. [10] - Nuclear Magnetic Resonance Methods for Quantifying Microsecond-to-Millisecond Motions in Biological Macromolecules. *Methods Enzymol.* **2001**, *339*, 204−238.
(53) Miller, J. M.; Brambley, C. A.; Marsee, J. D. Examination of the Role of Mg2+in the Mechanism of Nucleotide Binding to the Monomeric YME1L AAA+ Domain. *Biochemistry* **2020**, *59*, 4303−4320.
(54) Skinner, J. J.; Lim, W. K.; Bédard, S.; Black, B. E.; Englander, S. W. Protein hydrogen exchange: Testing current models. *Protein Sci.* **2012**, *21*, 987−995.
(55) Ye, X.; Lin, J.; Mayne, L.; Shorter, J.; Englander, S. W. Structural and kinetic basis for the regulation and potentiation of Hsp104 function. *Proc. Natl. Acad. Sci. U. S. A.* **2020**, *117*, 9384−9392.
(56) Konermann, L.; Rodriguez, A. D.; Sowole, M. A. Type 1 and Type 2 scenarios in hydrogen exchange mass spectrometry studies on protein−ligand complexes. *Analyst* **2014**, *139*, 6078−6087.
(57) Hanson, P. I.; Whiteheart, S. W. AAA+ proteins: Have engine, will work. *Nat. Rev. Mol. Cell Biol.* **2005**, *6*, 519−529.
(58) Sauer, R. T.; Baker, T. A. AAA+ Proteases: ATP-Fueled Machines of Protein Destruction. *Annurev Biochem.* **2011**, *80*, 587−612.
(59) Puchades, C.; Sandate, C. R.; Lander, G. C. The molecular principles governing the activity and functional diversity of AAA+ proteins. *Nat. Rev. Mol. Cell Biol.* **2020**, *21*, 43−58.
(60) Banerjee, S.; Bartesaghi, A.; Merk, A.; Rao, P.; Bulfer, S. L.; Yan, Y.; Green, N.; Mroczkowski, B.; Neitz, R. J.; Wipf, P.; Falconieri, V.; Deshaies, R. J.; Milne, J. L. S.; Huryn, D.; Arkin, M.; Subramaniam, S. 2.3 Å resolution cryo-EM structure of human p97 and mechanism of allosteric inhibition. *Science* **2016**, *351*, 871−875.
(61) Gerdes, F.; Tatsuta, T.; Langer, T. Mitochondrial AAA proteases - Towards a molecular understanding of membrane-bound proteolytic machines. *Biochim. Biophys. Acta, Mol. Cell Res.* **2012**, *1823*, 49−55.
(62) Ellman, G. L. Tissue Sulfhydryl Groups. *Arch. Biochem. Biophys.* **1959**, *82*, 70−77.
(63) Some, D. Light-scattering-based analysis of biomolecular interactions. *Biophys. Rev.* **2013**, *5*, 147−158.
(64) Gates, S. N.; Martin, A. Stairway to translocation: AAA+ motor structures reveal the mechanisms of ATP-dependent substrate translocation. *Protein Sci.* **2020**, *29*, 407−419.
(65) Khan, Y. A.; White, K. I.; Brunger, A. T. The AAA + superfamily: A review of the structural and mechanistic principles of these molecular machines. *Crit. Rev. Biochem. Mol. Biol.* **2022**, *57*, 156−187.
(66) Rainbolt, T. K.; Lebeau, J.; Puchades, C.; Wiseman, R. L. Reciprocal Degradation of YME1L and OMA1 Adapts Mitochondrial Proteolytic Activity during Stress. *Cell Rep.* **2016**, *14*, 2041−2049.
(67) Ye, X.; Lin, J.; Mayne, L.; Shorter, J.; Englander, S. W. Hydrogen exchange reveals Hsp104 architecture, structural dynamics, and energetics in physiological solution. *Proc. Natl. Acad. Sci. U. S. A.* **2019**, *116*, 7333−7342.
(68) Feng, Y.; Goncalves, M. M.; Jitkova, Y.; Keszei, A.; Sarathy, C.; Trudel, V.; St-Germain, J.; Tcheng, M.; Yan, Y.; Hurren, R.; Schultz, M.; Raught, B.; Yudin, A.; Mazhab-Jafari, M.; Vahidi, S.; Schimmer, A. D. Serine phosphorylation marks proteins for degradation by the mitochondrial matrix protease, ClpXP. *Cancer Res.* **2024**, *84*, 7053.
(69) Bieniossek, C.; Niederhauser, B.; Baumann, U. M. The crystal structure of apo-FtsH reveals domain movements necessary for substrate unfolding and translocation. *Proc. Natl. Acad. Sci. U. S. A.* **2009**, *106*, 21579−21584.
(70) Seraphim, T. V.; Houry, W. A. AAA+ proteins. *Curr. Biol.* **2020**, *30*, R251−R257.
(71) Pan, M.; Yu, Y.; Ai, H.; Zheng, Q.; Xie, Y.; Liu, L.; Zhao, M. Mechanistic insight into substrate processing and allosteric inhibition of human p97. *Nat. Struct Mol. Biol.* **2021**, *28*, 614−625.
(72) Iljina, M.; Mazal, H.; Dayananda, A.; Zhang, Z.; Stan, G.; Riven, I.; Haran, G. Single-molecule FRET probes allosteric effects on protein-translocating pore loops of a AAA+ machine. *Biophys. J.* **2024**, *123*, 374−388.
(73) Augustin, S.; Gerdes, F.; Lee, S.; Tsai, F. T. F.; Langer, T.; Tatsuta, T. An Intersubunit Signaling Network Coordinates ATP Hydrolysis by m-AAA Proteases. *Mol. Cell* **2009**, *35*, 574−585.
(74) Caffrey, B.; Zhu, X.; Berezuk, A.; Tuttle, K.; Chittori, S.; Subramaniam, S. AAA+ ATPase p97/VCP mutants and inhibitor binding disrupt inter-domain coupling and subsequent allosteric activation. *J. Biol. Chem.* **2021**, *297*, 101187.
(75) Huang, R.; Ripstein, Z. A.; Rubinstein, J. L.; Kay, L. E. Cooperative subunit dynamics modulate p97 function. *Proc. Natl. Acad. Sci. U. S. A.* **2019**, *116*, 158−167.
(76) Mickolajczyk, K. J.; Olinares, P. D. B.; Niu, Y.; Chen, N.; Warrington, S. E.; Sasaki, Y.; Walz, T.; Chait, B. T.; Kapoor, T. M. Long-range intramolecular allostery and regulation in the dynein-like AAA protein Mdn1. *Proc. Natl. Acad. Sci. U. S. A.* **2020**, *117*, 18459−18469.
(77) Mazal, H.; Iljina, M.; Barak, Y.; Elad, N.; Rosenzweig, R.; Goloubinoff, P.; Riven, I.; Haran, G. Tunable microsecond dynamics of an allosteric switch regulate the activity of a AAA+ disaggregation machine. *Nat. Commun.* **2019**, *10*, 1438.
(78) Shein, M.; Hitzenberger, M.; Cheng, T. C.; Rout, S. R.; Leitl, K. D.; Sato, Y.; Zacharias, M.; Sakata, E.; Schütz, A. K. Characterizing ATP processing by the AAA+ protein p97 at the atomic level. *Nat. Chem.* **2024**, *16*, 363−372.
(79) Shin, M.; Puchades, C.; Asmita, A.; Puri, N.; Adjei, E.; Wiseman, R. L.; Karzai, A. W.; Lander, G. C. Structural basis for distinct operational modes and protease activation in AAA+ protease Lon. *Sci. Adv.* **2020**, *6*, No. eaba8404.

https://doi.org/10.1021/acs.biochem.5c00535
Biochemistry XXXX, XXX, XXX−XXX